Sound wave resonances in Micro-Electro-Mechanical Systems devices vibrating at high frequencies according to the kinetic theory of gases

Laurent Desvillettes

ENS Cachan, CMLA, CNRS, PRES UniverSud & IUF, Cachan, France 94235

Silvia Lorenzani

Dipartimento di Matematica, Politecnico di Milano, Milano, Italy 20133

Abstract

The mechanism leading to gas damping in Micro-Electro-Mechanical Systems (MEMS) devices vibrating at high frequencies is investigated by using the linearized Boltzmann equation based on simplified kinetic models and diffuse reflection boundary conditions. Above a certain frequency of oscillation, the sound waves propagating through the gas are trapped in the gaps between the moving elements and the fixed boundaries of the microdevice. In particular, we found a scaling law, valid for all Knudsen numbers K_n (defined as the ratio between the gas mean free path and a characteristic length of the gas flow), that predicts a resonant response of the system. This response enables a minimization of the damping force exerted by the gas on the oscillating wall of the microdevice.

I. INTRODUCTION

In the last few years, Micro-Electro-Mechanical Systems (MEMS) devices vibrating at high frequencies (ranging from 1 MHz to 60 GHz) have increasingly been used in various industrial fields. In fact, such high frequency devices find applications in inertial sensing, acoustic transduction, optical signal manipulation and RF (radio frequency) components [1], [2], [3], [4], [5]. In particular, radio frequency microelectromechanical systems (RF MEMS) have become a major research area because they should enable a miniaturization and an integration of RF components, with applications to ultra low-power wireless and adaptive/secure telecommunications. In MEMS devices, the fluid is usually trapped under or around the vibrating micromechanical structure in extremely narrow gaps. As the structure vibrates, it pushes and pulls the fluid film creating complex pressure patterns that depend on the geometry of the structure, the boundary conditions, frequency of oscillations and thickness of the fluid film. In particular, when a planar microstructure oscillates in the direction perpendicular to its surface, the forces exerted by the fluid due to the built-up pressure are always against the movement of the structure. Thus, the fluid-film (typically air-film) acts as a damper and the phenomenon is called squeeze film damping. Low frequency MEMS devices are normally operated at very low pressure in order to minimize the damping due to the internal friction of the gas flowing in the small gaps between the moving parts of these microstructures [6], [7], [8], [9], [10]. This need can be overcome when MEMS devices vibrate at relatively high frequencies, since gas compressibility and inertial forces lead then to another damping mechanism which is related to the propagation of sound waves generated by high-frequency oscillating micro-structures. Very recently, the mechanism leading to gas damping in RF MEMS devices has been studied by using the linearized Navier-Stokes equations with slip boundary conditions for temperature in [11], [12]. Since the analysis presented in [11], [12] failed to predict the correct value of the damping force due to air in a RF MEMS disk resonator [1], [2], we report in the current paper a thorough study of time-periodic oscillatory flows encountered in MEMS devices vibrating at high frequency within the framework of kinetic theory of rarefied gas. In particular, we have found out a scaling law which predicts a resonant response of the system when the ratio between the rarefaction parameter

δ (inverse Knudsen number) and the dimensionless period of oscillation of the moving wall of the device takes a well-defined fixed value. The occurrence of an antiresonance is particularly important since if the device is operated close to the corresponding frequency, the damping due to the gas is considerably reduced. Since gas resonances take place for each value of δ, the RF MEMS devices can perform well also at atmospheric pressure greatly reducing the need for (and cost associated with) vacuum packaging.

II. MATHEMATICAL FORMULATION

Let us consider a monatomic gas confined in a three-dimensional rectangular section channel of dimensions Λ' in the x'-direction, W' in the y'-direction and d in the z'-direction. All the walls of the channel are held at the same constant temperature T_0. Assuming that the channel width W' is much larger than the other dimensions, the problem can be reduced to a two-dimensional one, as outlined in Fig. 1. The upper wall of the channel (located at $z' = d/2$) is fixed while the lower one (located at $z' = -d/2$) harmonically oscillates in the z'-direction (normal to the wall itself) with angular frequency ω' (the corresponding period being $T' = 2\pi/\omega'$). The velocity U'_w of the oscillating plate depends on time t' through the formula

$$U'_w(t') = U'_0 \sin(\omega' t') \tag{1}$$

where it is assumed that the amplitude U'_0 is very small compared to the thermal velocity v_0, i.e.

$$U'_0 << v_0, \qquad v_0 = \sqrt{2RT_0} \tag{2}$$

with R being the gas constant and T_0 being the equilibrium temperature of the gas. Under these conditions, the Boltzmann equation modeling the gas motion inside the channel can be linearized about a Maxwellian f_0 by putting [13], [14]

$$f = f_0(1 + h) \tag{3}$$

where $f(x', z', \mathbf{c}, t')$ is the distribution function for the molecular velocity $\mathbf{c}$ expressed in units of v_0 and $h(x', z', \mathbf{c}, t')$ is the small perturbation on the basic equilibrium state. The above mentioned Maxwellian function is given by

$$f_0 = \rho_0 \pi^{-\frac{3}{2}} \exp(-c^2) \tag{4}$$

where ρ_0 is the equilibrium density of the gas. Using Eq. (3), the nonstationary linearized Boltzmann equation reads as

$$\frac{\partial h}{\partial t'} + c_x \frac{\partial h}{\partial x'} + c_z \frac{\partial h}{\partial z'} = Lh \tag{5}$$

where Lh is the linearized collision operator. Since it is difficult to manage the Boltzmann operator L as such, for both analytical computations and numerical simulations, simplified kinetic models of the exact collision integral are widely used in practice. Because of its simplicity, the Bhatnagar, Gross and Krook (BGK) model is one of the most popular of these kinetic models [15], although it is known to have a serious flaw: it leads to a wrong Prandtl number (i.e. the dimensionless ratio of viscosity and thermal conductivity). This difficulty can be dealt with when one works in the linearized framework since viscosity and temperature effects are then decoupled [16], [17]. However, for the specific problem with which we are dealing here, where the sound waves generated by the oscillating plate propagate through the gas across the gap of the channel, both temperature variations and thermal conductivity must be accounted for due to compressibility effects. Thus, in order to correctly describe both mass and heat transfer, it is worth investigating the problem with a more refined model than the BGK. We shall therefore use the ellipsoidal statistical (ES) model, which allows to recover the right Prandtl number [18], [19], [20]. The linearized ES model gives rise to the following collision operator

$$Lh = \tilde{\theta}^{-1} \left[\rho + 2\mathbf{c} \cdot \mathbf{v} + \tau \left(\mathbf{c}^2 - 3/2 \right) - \lambda \, c_i \, c_j \, P_{ij} + \lambda \left(\rho + \tau \right) \mathbf{c}^2 / 2 - h \right] \tag{6}$$

where $\tilde{\theta}$ is a suitable mean free time, while the dimensionless macroscopic perturbed density ρ, velocity $\mathbf{v}$, temperature τ and stress tensor P_{ij} are obtained by taking the moments of h

$$\rho = \pi^{-3/2} \int_{-\infty}^{+\infty} h\, e^{-\mathbf{c}^2}\, d\mathbf{c}, \tag{7}$$

$$\mathbf{v} = \pi^{-3/2} \int_{-\infty}^{+\infty} \mathbf{c}\, h\, e^{-\mathbf{c}^2}\, d\mathbf{c}, \tag{8}$$

$$\tau = \pi^{-3/2} \int_{-\infty}^{+\infty} (\frac{2}{3}\mathbf{c}^2 - 1)\, h\, e^{-\mathbf{c}^2}\, d\mathbf{c}, \tag{9}$$

$$P_{ij} = \pi^{-3/2} \int_{-\infty}^{+\infty} c_i\, c_j\, h\, e^{-\mathbf{c}^2}\, d\mathbf{c}. \tag{10}$$

In Eq. (6), λ is a constant to be chosen in such a way that the correct Prandtl number is obtained, that is

$$P_r = c_p \frac{\mu}{k} \tag{11}$$

where c_p is the specific heat at constant pressure, μ the viscosity and k the thermal conductivity. λ is equal to 0 for the BGK model ($P_r = 1$) and 1 for a Maxwell gas ($P_r = 2/3$). For a general monoatomic gas the relation between λ and P_r is given by

$$P_r = \frac{2}{2+\lambda} \tag{12}$$

i.e.,

$$\lambda = \frac{2}{P_r} - 2 \tag{13}$$

In order to get the same viscosity coefficient from the BGK model and the present one, we must put

$$\tilde{\theta} = \frac{(\lambda+2)}{2}\theta \tag{14}$$

where $\theta = \mu/P_0$ is the collision time defined in the BGK model (with P_0 being the equilibrium pressure). It is convenient now to rescale all variables appearing in Eqs. (5) and (6) as follows

$$t = \frac{t'}{\theta}, \qquad x = \frac{x'}{v_0\theta}, \qquad z = \frac{z'}{v_0\theta} \tag{15}$$

so that the dimensionless ES linearized equation reads

$$\frac{\partial h}{\partial t} + c_x \frac{\partial h}{\partial x} + c_z \frac{\partial h}{\partial z} = \frac{2}{(2+\lambda)} \Bigg[\rho + 2\mathbf{c}\cdot\mathbf{v} + (\mathbf{c}^2 - 3/2)\,\tau - \lambda\, c_i\, c_j\, P_{ij} + \lambda\, \mathbf{c}^2(\rho+\tau)/2 - h \Bigg] \tag{16}$$

Appropriate boundary conditions must be supplied for the Boltzmann equation (16) to be solved. Assuming the diffuse scattering of gaseous particles on both walls (i.e., the reemitted molecules are diffused with a Maxwellian distribution described by the wall properties), the linearized boundary conditions, when $z = \pm\delta/2$, to be added to Eq. (16) have the following general expression [21], [22], [23]:

$$h(x, z=-\delta/2, \mathbf{c}, t) = (\sqrt{\pi} + 2\, c_z)\, U_w - \frac{2}{\pi} \int_{-\infty}^{\infty}\int_{-\infty}^{\infty} d\tilde{c}_x d\tilde{c}_y \int_{\tilde{c}_z<0} d\tilde{c}_z \tilde{c}_z\, e^{-\tilde{\mathbf{c}}^2}\, h(x, z=-\delta/2, \tilde{\mathbf{c}}, t) \quad c_z > 0 \tag{17}$$

$$h(x, z=\delta/2, \mathbf{c}, t) = \frac{2}{\pi} \int_{-\infty}^{\infty}\int_{-\infty}^{\infty} d\tilde{c}_x d\tilde{c}_y \int_{\tilde{c}_z>0} d\tilde{c}_z \tilde{c}_z\, e^{-\tilde{\mathbf{c}}^2}\, h(x, z=\delta/2, \tilde{\mathbf{c}}, t) \qquad c_z < 0 \tag{18}$$

where $\delta = d/(v_0\theta)$ is the rarefaction parameter (inverse Knudsen number), while at the channel entrance ($x = -\Lambda/2$) and exit ($x = \Lambda/2$) the ingoing part of the perturbed distribution function h vanishes. In Eq. (17), U_w is the dimensionless wall velocity given by

$$U_w(t) = U_0\, \sin(\omega\, t) \tag{19}$$

with $U_w = U_w'/v_0$, $U_0 = U_0'/v_0$, $\omega = \theta\,\omega'$, $T = 2\pi/\omega = T'/\theta$. Since the problem under consideration is two-dimensional, the unknown perturbed distribution function h, as well as the overall quantities, do not depend on the y coordinate. Moreover, we can also eliminate the c_y variable by introducing the following projection procedure [24], [25], [26]. First, we multiply Eq. (16) by $\frac{1}{\sqrt{\pi}}\, e^{-\mathbf{c_y}^2}$ and we integrate over all c_y. Then, we multiply Eq. (16) for a second time by $\frac{1}{\sqrt{\pi}}\,({c_y}^2 - 1/2)\, e^{-\mathbf{c_y}^2}$ and we integrate again over all c_y. The resulting equations after the projection are

$$\frac{\partial H}{\partial t} + c_x \frac{\partial H}{\partial x} + c_z \frac{\partial H}{\partial z} + \frac{2}{(2+\lambda)} H = \frac{2}{(2+\lambda)} \left[\rho + 2\, c_x\, v_x + 2\, c_z\, v_z + (c_x^2 + c_z^2 - 1)\, \tau \right.$$
$$\left. - \lambda\, (c_x^2 - 1/2)\, P_{xx} - \lambda\, (c_z^2 - 1/2)\, P_{zz} - 2\, \lambda\, c_x\, c_z\, P_{xz} + \frac{\lambda}{2}\, (c_x^2 + c_z^2 - 1)(\rho + \tau) \right] \quad (20)$$

and

$$\frac{\partial \Psi}{\partial t} + c_x \frac{\partial \Psi}{\partial x} + c_z \frac{\partial \Psi}{\partial z} + \frac{2}{(2+\lambda)} \Psi = \frac{2}{(2+\lambda)} \left[\frac{\tau}{2} - \frac{\lambda}{2}(\rho + \tau) + \frac{\lambda}{2}(P_{xx} + P_{zz}) \right] \quad (21)$$

where the reduced unknown distribution functions H and Ψ are defined as

$$H(x, z, c_x, c_z, t) = \frac{1}{\sqrt{\pi}} \int_{-\infty}^{+\infty} h(x, z, \mathbf{c}, t)\, e^{-c_y^2}\, dc_y \quad (22)$$

and

$$\Psi(x, z, c_x, c_z, t) = \frac{1}{\sqrt{\pi}} \int_{-\infty}^{+\infty} (c_y^2 - 1/2)\, h(x, z, \mathbf{c}, t)\, e^{-c_y^2}\, dc_y \quad (23)$$

respectively. In order to derive Eqs. (20) and (21) in their final form, we have considered the linearized equation of state

$$P = \frac{1}{3} \left[P_{xx} + P_{yy} + P_{zz} \right] = \frac{1}{2} (\rho + \tau) \quad (24)$$

with P being the dimensionless perturbed pressure of the gas. The macroscopic quantities appearing in the right-hand side of Eqs. (20) and (21) are defined by

$$\rho(x, z, t) = \frac{1}{\pi} \int_{-\infty}^{+\infty} \int_{-\infty}^{+\infty} H\, e^{-(c_x^2 + c_z^2)}\, dc_x dc_z \quad (25)$$

$$v_x(x, z, t) = \frac{1}{\pi} \int_{-\infty}^{+\infty} \int_{-\infty}^{+\infty} c_x\, H\, e^{-(c_x^2 + c_z^2)}\, dc_x dc_z \quad (26)$$

$$v_z(x, z, t) = \frac{1}{\pi} \int_{-\infty}^{+\infty} \int_{-\infty}^{+\infty} c_z\, H\, e^{-(c_x^2 + c_z^2)}\, dc_x dc_z \quad (27)$$

$$\tau(x, z, t) = \frac{1}{\pi} \int_{-\infty}^{+\infty} \int_{-\infty}^{+\infty} \frac{2}{3} \left[(c_x^2 + c_z^2 - 1)\, H + \Psi \right] e^{-(c_x^2 + c_z^2)}\, dc_x dc_z \quad (28)$$

$$P_{xx}(x,z,t) = \frac{1}{\pi}\int_{-\infty}^{+\infty}\int_{-\infty}^{+\infty} c_x^2\, H\, e^{-(c_x^2+c_z^2)}\, dc_x dc_z \tag{29}$$

$$P_{zz}(x,z,t) = \frac{1}{\pi}\int_{-\infty}^{+\infty}\int_{-\infty}^{+\infty} c_z^2\, H\, e^{-(c_x^2+c_z^2)}\, dc_x dc_z \tag{30}$$

$$P_{xz}(x,z,t) = \frac{1}{\pi}\int_{-\infty}^{+\infty}\int_{-\infty}^{+\infty} c_x\, c_z\, H\, e^{-(c_x^2+c_z^2)}\, dc_x dc_z \tag{31}$$

The elimination of one (or more) component of the molecular velocity by a projection procedure is quite important for the computational efficiency of the numerical scheme. The reduced distribution functions H and Ψ must satisfy the following boundary conditions coming from Eqs. (17) and (18):

$$H(x, z=-\delta/2, c_x, c_z, t) = (\sqrt{\pi} + 2\, c_z)\, U_w - \frac{2}{\sqrt{\pi}}\int_{-\infty}^{\infty} d\tilde{c}_x \int_{\tilde{c}_z<0} d\tilde{c}_z\, \tilde{c}_z\, e^{-(\tilde{c}_x^2+\tilde{c}_z^2)}\, H(x, z=-\delta/2, \tilde{c}_x, \tilde{c}_z, t) \quad c_z > 0 \tag{32}$$

$$\Psi(x, z=-\delta/2, c_x, c_z, t) = 0 \qquad c_z > 0 \tag{33}$$

$$H(x, z=\delta/2, c_x, c_z, t) = \frac{2}{\sqrt{\pi}}\int_{-\infty}^{\infty} d\tilde{c}_x \cdot \int_{\tilde{c}_z>0} d\tilde{c}_z\, \tilde{c}_z\, e^{-(\tilde{c}_x^2+\tilde{c}_z^2)}\, H(x, z=\delta/2, \tilde{c}_x, \tilde{c}_z, t) \qquad c_z < 0 \tag{34}$$

$$\Psi(x, z=\delta/2, c_x, c_z, t) = 0 \qquad c_z < 0 \tag{35}$$

To take into account also the transient behaviour of the sound waves excited by the forced oscillations of the channel wall, the time-dependent problem described by Eqs. (20) and (21), with boundary conditions given by Eqs. (32)-(35), has been numerically solved by a deterministic finite-difference method presented in detail in [27]. The numerical results show that above a certain frequency of oscillation, the sound wave propagation

takes place only in the z-direction across the gap, which indicates a fully trapped gas situation [11], [12]. This assumption greatly simplifies the analysis since the topology of the damper becomes insignificant and the problem can be reduced to a 1-dimensional one. To demonstrate the gas trapping in the channel gap at high frequencies, Figures 2-4 show the variations of the macroscopic fields of interest (obtained using the ES model) along the channel for different periods of oscillation. These frequencies represent different flow regimes that will be studied more closely in the next sections. The profiles reported in Figures 2-4 (at different stages during a period of oscillation after the transient behavior has ended) show clearly that, at high frequencies, the bulk flow velocity in the x-direction, v_x, and the xz-component of the stress tensor, P_{xz}, are zero (except very close to the borders, due to channel end effects) and the other macroscopic quantities (v_z and P_{zz}) do not depend on x. As frequencies decrease, the two-dimensional character of the flow field cannot be neglected and a full 2D description becomes mandatory in order to capture the correct magnitude of the macroscopic fields: This can be seen quite clearly in Figure 4, where the frequency is much lower than that in the other Figures. On physical grounds, one can observe that, since the velocity amplitude U_0 is fixed, the displacement amplitude of the plate (U_0/ω) decreases as the frequency ω increases. This means that, at very high frequencies, the gas is not squeezed between the two walls and a flow parallel to the bounding plates of the channel cannot arise. Figures 2-4 have been obtained by considering a specific value of the rarefaction parameter ($\delta = 0.1$) but the shape of the macroscopic-fields profiles remains qualitatively and quantitatively the same if one changes δ and T in such a way that the ratio δ/T is kept constant. This means that, if for $\delta = 0.1$ the transition to a two-dimensional flow field requires $T > 0.5$, for $\delta = 1$ one should have $T > 5$, and for $\delta = 10$ $T > 50$. This aspect will be fully clarified in the next section.

III. ONE-DIMENSIONAL SOUND WAVE PROPAGATION MODEL

When the frequency of oscillation in a squeezed-film damper is sufficiently high for the gas to be trapped in the channel gap, the basic kinetic equations (20) and (21) degenerate to the following set

$$\frac{\partial H}{\partial t} + c_z \frac{\partial H}{\partial z} + \frac{2}{(2+\lambda)} H = \frac{2}{(2+\lambda)} \Bigg[\rho + 2\, c_z\, v_z + (c_z^2 - 1/2)\, \tau - \lambda\, (c_z^2 - 1/2)\, P_{zz} + \frac{\lambda}{2}\, (c_z^2 - 1/2)(\rho + \tau) \Bigg] \tag{36}$$

and

$$\frac{\partial \Psi}{\partial t} + c_z \frac{\partial \Psi}{\partial z} + \frac{2}{(2+\lambda)} \Psi = \frac{2}{(2+\lambda)} \left[\tau - \frac{\lambda}{4}(\rho + \tau) + \frac{\lambda}{2} P_{zz} \right] \tag{37}$$

where now the reduced unknown distribution functions H and Ψ are expressed as

$$H(z, c_z, t) = \frac{1}{\pi} \int_{-\infty}^{+\infty} \int_{-\infty}^{+\infty} h(z, \mathbf{c}, t)\, e^{-(c_x^2 + c_y^2)}\, dc_x\, dc_y \tag{38}$$

and

$$\Psi(z, c_z, t) = \frac{1}{\pi} \int_{-\infty}^{+\infty} \int_{-\infty}^{+\infty} (c_x^2 + c_y^2 - 1)\, h(z, \mathbf{c}, t)\, e^{-(c_x^2 + c_y^2)}\, dc_x\, dc_y \tag{39}$$

respectively. The macroscopic fields appearing on the right-hand side of Eqs. (36) and (37) are defined by

$$\rho(z, t) = \frac{1}{\sqrt{\pi}} \int_{-\infty}^{+\infty} H\, e^{-c_z^2}\, dc_z \tag{40}$$

$$v_z(z, t) = \frac{1}{\sqrt{\pi}} \int_{-\infty}^{+\infty} c_z\, H\, e^{-c_z^2}\, dc_z \tag{41}$$

$$\tau(z, t) = \frac{1}{\sqrt{\pi}} \int_{-\infty}^{+\infty} \frac{2}{3} \Big[(c_z^2 - 1/2)\, H + \Psi \Big]\, e^{-c_z^2}\, dc_z \tag{42}$$

$$P_{zz}(z, t) = \frac{1}{\sqrt{\pi}} \int_{-\infty}^{+\infty} c_z^2\, H\, e^{-c_z^2}\, dc_z \tag{43}$$

while the linearized boundary conditions (32)-(35) become

$$H(z = -\delta/2, c_z, t) = (\sqrt{\pi} + 2\, c_z)\, U_w - 2 \int_{\tilde{c}_z < 0} d\tilde{c}_z\, \tilde{c}_z\, e^{-\tilde{c}_z^2}\, H(z = -\delta/2, \tilde{c}_z, t) \qquad c_z > 0 \tag{44}$$

$$\Psi(z=-\delta/2,c_z,t)=0 \qquad c_z>0 \qquad (45)$$

$$H(z=\delta/2,c_z,t)=2\int_{\tilde{c}_z>0} d\tilde{c}_z\,\tilde{c}_z\,e^{-\tilde{c}_z^2}\,H(z=\delta/2,\tilde{c}_z,t) \qquad c_z<0 \qquad (46)$$

$$\Psi(z=\delta/2,c_z,t)=0 \qquad c_z<0 \qquad (47)$$

In order to compute the force exerted by the gas on the moving wall of the channel, the perturbation of the normal stress P_{zz} (defined by Eq. (43)) has to be evaluated at $z=-\delta/2$. Therefore, to validate our numerical code, we list in Tables I and II the values of the amplitude and of the phase of P_{zz} at the oscillating wall, obtained through a numerical integration of Eqs. (36) and (37), along with the highly accurate results obtained in [26] from a numerical solution of the linearized Shakhov kinetic equation. The normal stress time-dependence is of the following known form:

$$|P_{zz}|\,\sin(\omega\,t+\phi) \qquad (48)$$

where $|P_{zz}|$ is the amplitude and ϕ the phase. In general, the amplitude of the time-dependent macroscopic fields is extracted from our numerical results as half the vertical distance between a maximum and the nearest minimum appearing in the temporal evolution of the macroscopic quantity. This corresponds to the definition

$$|A(z,t)|=[\mathcal{R}e(A)^2+\mathcal{I}m(A)^2]^{1/2} \qquad (49)$$

where $\mathcal{R}e$ and $\mathcal{I}m$ denote the real and imaginary part, respectively, of the field $A(z,t)$. Instead, the phase can be recovered from our simulations through the application of a chi-square fit to the functional form of the expression (48) [28], [29].

Even if, in the context of our work, the interest is focused on micro-devices vibrating at high frequencies (where the problem is reduced to a 1-dimensional one due to the gas trapping in the channel gap), we have listed in Tables I and II three different values of the

period T, which cover all oscillation regimes only for the sake of comparison with the outputs reported in [26] (where the one-dimensional description arises, on the contrary, from the double degenerate geometry considered, that is, infinitely long and wide channels). Then, for each T, several values of the rarefaction parameter δ, lying in the transitional region, have been taken into account. As shown in the tables, the agreement between the numerical results obtained in [26] by using the Shakhov model and our outputs based on both BGK and ES kinetic models is fairly good. This comparison reveals not only the reliability of our numerical method of solution, but also the weak dependence of the normal stress field evaluated at the moving channel wall on the collisional model used. This last point will be discussed more deeply in Section IV.

Low frequency MEMS devices are normally operated at very low pressure in order to minimize the damping due to gas flow in the small gaps between the moving parts of these microstructures. This need can be overcome when MEMS devices vibrate at relatively high frequencies, since gas compressibility and inertial forces lead then to another damping mechanism (in addition to the viscous damping that dominates at low frequencies). In particular, inertial forces will cause a gas resonance in the z-direction when the dimensionless distance between the channel walls (measured in units of the oscillation period of the moving plate)

$$L = \frac{\delta}{T} = \frac{d\,\omega'}{2\,\pi\,v_0} \tag{50}$$

takes a well-defined fixed value. Note that the quantity $(2\,\pi\,v_0/\omega')$ is the distance traveled by gaseous molecules during one cycle of oscillation of the moving boundary. Corresponding to a resonant response of the system, the amplitude of P_{zz} at $z = -\delta/2$ reaches its maximum value (resonance) or its minimum value (antiresonance). This is illustrated in Fig. 5, which shows the temporal evolution of $P_{zz}(z = -\delta/2, t)$ (obtained using the ES model), after the transient behavior has ended, for different periods of oscillation of the moving wall. This picture has been obtained by considering a specific value of the rarefaction parameter ($\delta = 0.1$) but the profiles of $P_{zz}(z = -\delta/2, t)$ show an analogous trend for each value of δ. The occurrence of an antiresonance is particularly important since if the device is operated close to the corresponding frequency, the damping due to

the gas (measured by the amplitude of $P_{zz}(z=-\delta/2,t)$) is considerably reduced. As a consequence, an analytical expression for P_{zz} is highly desirable if one wants to be able to predict the occurrence of the gas resonances. In order to simplify the analytical treatment, one can take advantage of a result discussed in Section IV, that is, the thermal effects on the flow field can be neglected for periods, T, of oscillations of the channel wall such that $T \lesssim 1$. When this condition is fulfilled, it can be shown, furthermore, (cf. Section IV) that there is only a weak dependence of the problem on the chosen intermolecular collision model and the analytical treatment of the problem can be performed with the following simplified BGK equation

$$\frac{\partial H}{\partial t} + c_z \frac{\partial H}{\partial z} + H = \rho + 2\, c_z\, v_z \tag{51}$$

obtained from Eqs. (36) and (37) by choosing $\lambda = 0$ and by dropping out the term related to thermal perturbations. In Eq. (51), ρ and v_z are still given by Eqs. (40) and (41), respectively, and the boundary conditions (44) and (46) are imposed. Since the vibrations of the system are generated by a time-harmonic forcing (of frequency ω) of the form $\sin(\omega\, t)$ (see Eq. (19)), we introduce the following expression $U_w = U_0\, e^{i\,\omega t}$ in Eq. (44) and then we look for solutions of Eq. (51) under the form

$$H(z, c_z, t) = \mathcal{H}(z, c_z)\, e^{i\,\omega\, t}. \tag{52}$$

The solutions of the original problem (where $U_w = U_0\, \sin(\omega\, t)$) are then recovered by taking the imaginary part of H. Inserting Eq. (52) in (51), the BGK model equation reads

$$c_z \frac{\partial \mathcal{H}}{\partial z}(z, c_z) + (1 + i\,\omega)\, \mathcal{H}(z, c_z) = \varrho(z) + 2\, c_z\, \mathrm{v}_z(z) \tag{53}$$

where

$$\varrho(z) = \rho(z,t) e^{-i\,\omega\, t} = \frac{1}{\sqrt{\pi}} \int_{-\infty}^{\infty} \mathcal{H}(z, c_z)\, e^{-c_z^2}\, dc_z \tag{54}$$

$$\mathrm{v}_z(z) = v_z(z,t) e^{-i\,\omega\, t} = \frac{1}{\sqrt{\pi}} \int_{-\infty}^{\infty} c_z\, \mathcal{H}(z, c_z)\, e^{-c_z^2}\, dc_z \tag{55}$$

The boundary conditions to be added to Eq. (53) are derived from Eqs. (44) and (46) under the assumption (52) and the choice of the forcing term: $U_w = e^{i\,\omega\,t}$ (where we have fixed $U_0 = 1$, which is not restrictive within the framework of a linearized analysis). It is somewhat more convenient to rewrite the boundary conditions in the form [21]

$$\mathcal{H}(z = -\delta/2, c_z > 0) = B_1 + 2\,c_z \tag{56}$$

$$\mathcal{H}(z = \delta/2, c_z < 0) = B_2 \tag{57}$$

where

$$B_1 = \sqrt{\pi} - 2\int_{\tilde{c_z}<0} \mathcal{H}(z = -\delta/2, \tilde{c_z})\,\tilde{c_z}\,e^{-\tilde{c_z}^2}\,d\tilde{c_z} \tag{58}$$

$$B_2 = 2\int_{\tilde{c_z}>0} \mathcal{H}(z = \delta/2, \tilde{c_z})\,\tilde{c_z}\,e^{-\tilde{c_z}^2}\,d\tilde{c_z} \tag{59}$$

Integrating now Eq. (53) along the trajectories of the molecules, we get

$$\begin{aligned}\mathcal{H}(z, c_z) = e^{-\frac{z}{c_z}\,\gamma}\,e^{-\frac{\delta\,\mathrm{sgn}c_z}{2\,c_z}\,\gamma}\mathcal{H}(-\delta/2\,\mathrm{sgn}c_z, c_z) \\ + \int_{-\delta/2\,\mathrm{sgn}c_z}^{z} ds\,[\varrho(s) + 2\,c_z\,\mathrm{v}_z(s)]/c_z\,e^{-|z-s|\,\frac{\gamma}{|c_z|}}\end{aligned} \tag{60}$$

with $\gamma = (1 + i\,\omega)$. Enforcing Eq. (60) at the boundaries, one obtains two equations:

$$\mathcal{H}^-(z = -\delta/2, c_z) = e^{\frac{\delta}{c_z}\,\gamma}\,B_2 + \int_{-\delta/2}^{\delta/2} ds\,[\varrho(s) - 2\,|c_z|\,\mathrm{v}_z(s)]/|c_z|\,e^{-(\delta/2+s)\,\frac{\gamma}{|c_z|}} \tag{61}$$

$$\begin{aligned}\mathcal{H}^-(z = \delta/2, c_z) = e^{-\frac{\delta}{c_z}\,\gamma}\,(B_1 + 2\,c_z) \\ + \int_{-\delta/2}^{\delta/2} ds\,[\varrho(s) + 2\,c_z\,\mathrm{v}_z(s)]/c_z\,e^{-(\delta/2-s)\,\frac{\gamma}{c_z}}\end{aligned} \tag{62}$$

where $\mathcal{H}^-(z = -\delta/2, c_z)$, $\mathcal{H}^-(z = \delta/2, c_z)$ are the distribution functions of the molecules impinging upon the walls. By using Eqs. (61) and (62), after standard manipulations, the expression of B_1 and B_2 can be explicitly written as

$$B_1 = [1 - 4\,T_1^2(\delta\,\gamma)]^{-1} \left\{ \sqrt{\pi} + 8\,T_1(\delta\,\gamma)\,T_2(\delta\,\gamma) \right.$$
$$+ \int_{-\delta/2}^{\delta/2} ds\,\varrho(s)\,[4\,T_1(\delta\,\gamma)\,T_0((\delta/2 - s)\,\gamma) + 2\,T_0((\delta/2 + s)\,\gamma)]$$
$$\left. + \int_{-\delta/2}^{\delta/2} ds\,\mathrm{v}_z(s)\,[8\,T_1(\delta\,\gamma)\,T_1((\delta/2 - s)\,\gamma) - 4\,T_1((\delta/2 + s)\,\gamma)] \right\} \tag{63}$$

and

$$B_2 = [1 - 4\,T_1^2(\delta\,\gamma)]^{-1} \left\{ 2\,\sqrt{\pi}\,T_1(\delta\,\gamma) + 4\,T_2(\delta\,\gamma) \right.$$
$$+ \int_{-\delta/2}^{\delta/2} ds\,\varrho(s)\,[4\,T_1(\delta\,\gamma)\,T_0((\delta/2 + s)\,\gamma) + 2\,T_0((\delta/2 - s)\,\gamma)]$$
$$\left. + \int_{-\delta/2}^{\delta/2} ds\,\mathrm{v}_z(s)\,[4\,T_1((\delta/2 - s)\,\gamma) - 8\,T_1(\delta\,\gamma)\,T_1((\delta/2 + s)\,\gamma)] \right\} \tag{64}$$

where T_n denotes the Abramowitz functions defined by

$$T_n(x) := \int_0^{+\infty} s^n\,e^{-s^2 - x/s}\,ds. \tag{65}$$

Inserting in the definitions (54) and (55) the distribution function (60), together with the boundary conditions (56) and (57), the density ϱ and the bulk velocity v_z of the gas are seen to satisfy the following equations:

$$\varrho(z) = \frac{2}{\sqrt{\pi}}\, T_1((\delta/2+z)\,\gamma) + \frac{1}{\sqrt{\pi}}\,[1-4\,T_1^2(\delta\,\gamma)]^{-1}\,T_0((\delta/2-z)\,\gamma)\,[2\sqrt{\pi}\,T_1(\delta\,\gamma)+4\,T_2(\delta\,\gamma)]$$
$$+\frac{1}{\sqrt{\pi}}\,[1-4\,T_1^2(\delta\,\gamma)]^{-1}\,T_0((\delta/2+z)\,\gamma)\,[\sqrt{\pi}+8\,T_1(\delta\,\gamma)\,T_2(\delta\,\gamma)]$$
$$+\frac{1}{\sqrt{\pi}}\int_{-\delta/2}^{\delta/2} ds\,\varrho(s)\,T_{-1}(|z-s|\,\gamma) + \frac{1}{\sqrt{\pi}}\,[1-4\,T_1^2(\delta\,\gamma)]^{-1}\int_{-\delta/2}^{\delta/2} ds\,\varrho(s)\,\cdot$$
$$\Big[4\,T_1(\delta\,\gamma)\,T_0((\delta/2-z)\,\gamma)\,T_0((\delta/2+s)\,\gamma)+2\,T_0((\delta/2-z)\,\gamma)\,T_0((\delta/2-s)\,\gamma)$$
$$+4\,T_1(\delta\,\gamma)\,T_0((\delta/2+z)\,\gamma)\,T_0((\delta/2-s)\,\gamma)+2\,T_0((\delta/2+z)\,\gamma)\,T_0((\delta/2+s)\,\gamma)\Big]$$
$$+\frac{2}{\sqrt{\pi}}\int_{-\delta/2}^{\delta/2} ds\,\mathrm{v}_z(s)\,sgn(z-s)\,T_0(|z-s|\,\gamma)+\frac{1}{\sqrt{\pi}}\,[1-4\,T_1^2(\delta\,\gamma)]^{-1}\int_{-\delta/2}^{\delta/2} ds\,\mathrm{v}_z(s)\,\cdot$$
$$\Big[4\,T_0((\delta/2-z)\,\gamma)\,T_1((\delta/2-s)\,\gamma)-8\,T_1(\delta\,\gamma)\,T_0((\delta/2-z)\,\gamma)\,T_1((\delta/2+s)\,\gamma)$$
$$+8\,T_1(\delta\,\gamma)\,T_0((\delta/2+z)\,\gamma)\,T_1((\delta/2-s)\,\gamma)-4\,T_0((\delta/2+z)\,\gamma)\,T_1((\delta/2+s)\,\gamma)\Big] \quad (66)$$

and

$$\mathrm{v}_z(z) = \frac{2}{\sqrt{\pi}}\, T_2((\delta/2+z)\,\gamma) - \frac{1}{\sqrt{\pi}}\,[1-4\,T_1^2(\delta\,\gamma)]^{-1}\,T_1((\delta/2-z)\,\gamma)\,[2\sqrt{\pi}\,T_1(\delta\,\gamma)+4\,T_2(\delta\,\gamma)]$$
$$+\frac{1}{\sqrt{\pi}}\,[1-4\,T_1^2(\delta\,\gamma)]^{-1}\,T_1((\delta/2+z)\,\gamma)\,[\sqrt{\pi}+8\,T_1(\delta\,\gamma)\,T_2(\delta\,\gamma)]$$
$$+\frac{1}{\sqrt{\pi}}\int_{-\delta/2}^{\delta/2} ds\,\varrho(s)\,sgn(z-s)\,T_0(|z-s|\,\gamma) - \frac{1}{\sqrt{\pi}}\,[1-4\,T_1^2(\delta\,\gamma)]^{-1}\int_{-\delta/2}^{\delta/2} ds\,\varrho(s)\,\cdot$$
$$\Big[4\,T_1(\delta\,\gamma)\,T_1((\delta/2-z)\,\gamma)\,T_0((\delta/2+s)\,\gamma)+2\,T_1((\delta/2-z)\,\gamma)\,T_0((\delta/2-s)\,\gamma)$$
$$-4\,T_1(\delta\,\gamma)\,T_1((\delta/2+z)\,\gamma)\,T_0((\delta/2-s)\,\gamma)-2\,T_1((\delta/2+z)\,\gamma)\,T_0((\delta/2+s)\,\gamma)\Big]$$
$$+\frac{2}{\sqrt{\pi}}\int_{-\delta/2}^{\delta/2} ds\,\mathrm{v}_z(s)\,T_1(|z-s|\,\gamma)-\frac{1}{\sqrt{\pi}}\,[1-4\,T_1^2(\delta\,\gamma)]^{-1}\int_{-\delta/2}^{\delta/2} ds\,\mathrm{v}_z(s)\,\cdot$$
$$\Big[4\,T_1((\delta/2-z)\,\gamma)\,T_1((\delta/2-s)\,\gamma)-8\,T_1(\delta\,\gamma)\,T_1((\delta/2-z)\,\gamma)\,T_1((\delta/2+s)\,\gamma)$$
$$-8\,T_1(\delta\,\gamma)\,T_1((\delta/2+z)\,\gamma)\,T_1((\delta/2-s)\,\gamma)+4\,T_1((\delta/2+z)\,\gamma)\,T_1((\delta/2+s)\,\gamma)\Big] \quad (67)$$

Eqs. (66) and (67) form a system of two coupled integral equations for $\varrho(z)$ and $\mathrm{v}_z(z)$. The perturbation of the normal stress P_{zz} (evaluated at $z=-\delta/2$), which has a direct connection with the damping force exerted by the gas on the moving wall of the channel, can be expressed in terms of the density and the bulk velocity of the gas as follows:

$$\mathcal{P}_{zz}(z=-\delta/2) = P_{zz}(z=-\delta/2,t)\,e^{-i\,\omega\,t} = \frac{1}{\sqrt{\pi}} + [1-4\,T_1^2(\delta\,\gamma)]^{-1}\cdot$$
$$\left[\frac{\sqrt{\pi}}{4} + \frac{4}{\sqrt{\pi}}\,T_2^2(\delta\,\gamma) + 4\,T_1(\delta\,\gamma)\,T_2(\delta\,\gamma)\right] + \frac{1}{\sqrt{\pi}}\int_{-\delta/2}^{\delta/2} ds\,\varrho(s)\,T_1(|-\delta/2-s|\,\gamma)$$
$$+\frac{1}{\sqrt{\pi}}\,[1-4\,T_1^2(\delta\,\gamma)]^{-1}\left[\frac{\sqrt{\pi}}{2} + 4T_2(\delta\,\gamma)\,T_1(\delta\,\gamma)\right]\int_{-\delta/2}^{\delta/2} ds\,\varrho(s)\,T_0((\delta/2+s)\,\gamma)$$
$$+\frac{1}{\sqrt{\pi}}\,[1-4\,T_1^2(\delta\,\gamma)]^{-1}[2\,T_2(\delta\,\gamma)+\sqrt{\pi}\,T_1(\delta\,\gamma)]\int_{-\delta/2}^{\delta/2} ds\,\varrho(s)\,T_0((\delta/2-s)\,\gamma)$$
$$+\frac{2}{\sqrt{\pi}}\int_{-\delta/2}^{\delta/2} ds\,\mathrm{v}_z(s)\,sgn(-\delta/2-s)\,T_2(|-\delta/2-s|\,\gamma) + \frac{2}{\sqrt{\pi}}\,[1-4\,T_1^2(\delta\,\gamma)]^{-1}\cdot$$
$$[2\,T_2(\delta\,\gamma)+\sqrt{\pi}\,T_1(\delta\,\gamma)]\int_{-\delta/2}^{\delta/2} ds\,\mathrm{v}_z(s)\,T_1((\delta/2-s)\,\gamma) - \frac{2}{\sqrt{\pi}}\,[1-4\,T_1^2(\delta\,\gamma)]^{-1}\cdot$$
$$[4\,T_2(\delta\,\gamma)T_1(\delta\,\gamma)+\sqrt{\pi}/2]\int_{-\delta/2}^{\delta/2} ds\,\mathrm{v}_z(s)\,T_1((\delta/2+s)\,\gamma) \tag{68}$$

As previously mentioned, in order to get a solution to the original problem with a forcing of the form $\sin(\omega t)$, one needs to take the imaginary part of the time-dependent macroscopic fields: $\rho(z,t)$, $v_z(z,t)$, $P_{zz}(z,t)$. Furthermore, it is worth noting that any absolute constant can be added to the solution obtained here, and this still gives a solution to the problem. Thus, the evaluation of the damping exerted by the gas on the moving wall of the channel has been reduced to the task of solving the integral equations (66) and (67). To this end, we extend a finite difference technique first introduced in a paper by Cercignani and Daneri [30]. The one-dimensional computational domain is divided into n mesh points (for simplicity, only constant mesh steps are considered) and the macroscopic fields ($\varrho(z)$ and $\mathrm{v}_z(z)$) are approximated by a stepwise function. The general form of the numerical scheme is given by [31]

$$\sum_{k=0}^{2\,n-1} \alpha_{hk}\psi_k = \beta_h \qquad\qquad (h=0,\ldots,2\,n-1) \tag{69}$$

where

$$\psi_i = \varrho(z_i) \qquad\qquad (i=0,\ldots,n-1) \tag{70}$$

$$\psi_{i+n} = \mathrm{v}_z(z_i) \qquad\qquad (i=0,\ldots,n-1) \tag{71}$$

Following the idea reported in [30], the constant value assigned to the functions $\varrho(z)$ and $\mathrm{v}_z(z)$ on every interval can be interpreted as either (a) the value in the midpoint or (b) the mean value on the whole interval, so that two methods of differencing can be defined with two possible choices for the coefficients α_{hk} and β_h. In the APPENDIX, we report only the coefficients related to the method of differencing (a) (which can be computed more easily), since with a resolution of $n = 200$ mesh points (used in the present computations to reach very high accuracy), the two schemes approach so closely each other that they can be considered equivalent.

It has been verified that the agreement between the profiles of the macroscopic fields given by Eqs. (66)-(68) and the results based on the kinetic equations (36) and (37) by choosing $\lambda = 0$ is very good (the relative error is less than 0.5%) in the entire range of validity of the formulas (66)-(68), that is $T \lesssim 1$ and arbitrary Knudsen numbers.

IV. RESONANT FREQUENCIES

Since the resonances take place when the ratio between the gap dimensions and the distance traveled by the molecules during one cycle of the oscillations of the moving boundary assumes a fixed value (see Eq. (50)), we restrict ourselves to gas flow conditions which allow to compute such a value by a simple procedure. In the limit $\delta << 1$, the integrals appearing in Eq. (68) vanish and the only term for which we have to find the maxima and minima is

$$f(\omega) = [1 - 4\,T_1^2(\delta\,(1+i\omega))]^{-1}\left[\frac{\sqrt{\pi}}{4} + \frac{4}{\sqrt{\pi}}\,T_2^2(\delta\,(1+i\omega)) + 4\,T_1(\delta\,(1+i\omega))\,T_2(\delta\,(1+i\omega))\right] \tag{72}$$

Still writing $\gamma = 1 + i\omega$, it amounts to finding the zeros of the derivative of f with respect to ω, that is, the zeros of the following function

$$F(\gamma) = \frac{8\,\delta}{\sqrt{\pi}}\,T_1(\delta\,\gamma)\,T_2(\delta\,\gamma) + 4\,\delta\,T_0(\delta\,\gamma)\,T_2(\delta\,\gamma) + 4\,\delta\,T_1^2(\delta\,\gamma)$$
$$- \frac{32\,\delta}{\sqrt{\pi}}\,T_1^3(\delta\,\gamma)\,T_2(\delta\,\gamma) + 16\,\delta\,T_0(\delta\,\gamma)\,T_1^2(\delta\,\gamma)\,T_2(\delta\,\gamma) - 16\,\delta\,T_1^4(\delta\,\gamma)$$
$$+ 2\,\sqrt{\pi}\delta\,T_0(\delta\,\gamma)\,T_1(\delta\,\gamma) + \frac{32\,\delta}{\sqrt{\pi}}\,T_0(\delta\,\gamma)\,T_1(\delta\,\gamma)\,T_2^2(\delta\,\gamma) \tag{73}$$

Indeed, due to the choice of the forcing term in the analytical treatment (as underlined in the previous section), we will consider only the zeros of the imaginary part of F. Then, once the stationary points of $f(\omega)$ have been found, the sign of the second derivative of f with respect to ω allows to distinguish if the stationary point is a maximum (resonance) or a minimum (antiresonance). Figure 6 shows the variation of the imaginary part of F as a function of the period T for a fixed value of the rarefaction parameter $\delta = 0.01$, satisfying the condition $\delta << 1$ under which Eq. (73) has been derived. The picture reveals that there are many zeros of the imaginary part of the function F, two of them corresponding to the main resonances located at:

$$T_a \simeq 4.7\,10^{-2} \quad \text{(antiresonance)} \tag{74}$$

$$T_r \simeq 2.1\,10^{-2} \quad \text{(resonance)} \tag{75}$$

and leading to the values $L_a \simeq 0.21$ and $L_r \simeq 0.48$, respectively, for the dimensionless distance between the channel walls (see Eq. (50)). The zeros corresponding to smaller values of T are related to higher-order resonances. Indeed, the values given by the formulas (74) and (75) are not the exact zeros of the function plotted in Fig. 6 but a sort of weighted average between the analytical results and the numerical outcomes, presented in Figs. 7-9, which show slight deviations from the findings obtained by using Eq. (73). Once the approximated fixed values, L_a and L_r, have been determined by using Eq. (73), which holds under the condition $\delta << 1$ and $T \lesssim 1$ (that is, negligible thermal effects), Eq. (50) allows to compute the values of T for the occurrence of resonances and antiresonances for different values of the rarefaction parameter δ progressing from free molecular, through transitional, to continuum regions (since the ratio δ/T must assume always the same constant value, each time the system undergoes a resonant response, if one believes that Eq. (50) should express a scaling law).

In order to test the reliability of the analytical formula (73) to predict the occurrence of resonances, Figures 7-9 show the profiles of the normal stress amplitude at the oscillating wall, obtained by numerical integration of Eqs. (36) and (37), as a function of the period T, for three different values of the rarefaction parameter δ. We have included in these pictures results based on the BGK model and the ES model along with the outputs obtained by numerical integration of the BGK equation (51), where the thermal perturbations have been dropped out. This is done to assess the influence of the collision model as well as the thermal effects on the damping force exerted by the gas on the moving channel wall.

From Figures 7-9, one can conclude the following.

(i) The location of the main resonance (resp. antiresonance) which corresponds to the highest maximum (resp. lowest minimum) is well predicted by the analytical formula (73) for each value of the rarefaction parameter. In fact, Eq. (50), applied by considering the values of L analytically derived through Eq. (73) (that is, $L_a \simeq 0.21$ and $L_r \simeq 0.48$), predicts the following values of T corresponding to the occurrence of resonances (T_r) and antiresonances (T_a), for the three different values of the rarefaction parameter δ used in Figs. 7-9:

$$\delta = 0.1 \Longrightarrow T_r = \frac{\delta}{L_r} = \frac{0.1}{0.48} \simeq 0.21$$
$$T_a = \frac{\delta}{L_a} = \frac{0.1}{0.21} \simeq 0.47$$

$$\delta = 1 \Longrightarrow T_r = \frac{\delta}{L_r} = \frac{1}{0.48} \simeq 2.1$$
$$T_a = \frac{\delta}{L_a} = \frac{1}{0.21} \simeq 4.7$$

$$\delta = 10 \Longrightarrow T_r = \frac{\delta}{L_r} = \frac{10}{0.48} \simeq 21$$
$$T_a = \frac{\delta}{L_a} = \frac{10}{0.21} \simeq 47$$

These values are in good agreement with the numerical results presented in Figs. 7-9.

All the other local maxima (resp. minima) appearing in the pictures are related to higher-order resonances (which are also well predicted by the formula (73)) since the values taken by $|P_{zz}(z = -\delta/2)|$ at each maximum (minimum) decrease (increase) as the period T goes to zero.

(ii) The influence of the collisional model on the normal stress amplitude evaluated at the moving wall is negligible for each rarefaction parameter δ in the free-molecular limit and in the transitional region, while a slight deviation between the BGK and ES models is evident in a neighbourhood of the main resonance in the near-continuum regime. While it is expected that the influence of a collisional model should increase in the continuum limit, nevertheless the appearance of this discrepancy only near the highest maximum of the normal stress amplitude profile leads to infer that this deviation between the two kinetic models could be related to the start-up of nonlinear effects. In fact, it is worth noting that, the value of $|P_{zz}(z = -\delta/2)|$ corresponding to the main resonant frequency increases with increasing δ. However, both kinetic models (BGK and ES) leave the location of the resonances (antiresonances) practically unchanged. In the problem at hand here, the occurrence of the main antiresonance is of particular interest since if the device is operated close to this frequency, a very small damping due to the gas can be achieved. In particular, Figures 7-9 show that the value of $|P_{zz}(z = -\delta/2)|$ corresponding to the main antiresonant frequency decreases by increasing δ. Therefore, squeezed-film dampers vibrating at high frequencies, unlike the low frequency MEMS devices, do not need to operate at very low pressure in order to minimize the damping due to gas flow.

(iii) The thermal effects do not play any role in determining the amplitude of the normal stress at the moving wall, $|P_{zz}(z = -\delta/2)|$, when the plate oscillates with high frequency (i.e. $T \lesssim 1$), while they dominate at lower frequencies. This means that for a rarefaction parameter $\delta > 1$ (which requires a period of oscillation $T > 1$ in order to detect the occurrence of the main resonances), it is important to include the full temperature dependence in the model in order to predict the exact location of the resonances as well as the correct amplitude of the normal stress.

On experimental grounds, it is unfeasible to detect a resonant response of the system

by putting a microphone on a plate vibrating at high frequencies in order to measure the acoustic pressure directly on the sound waves source. The numerical simulations suggest an alternative approach that relies on showing a peculiar feature characterizing the flow field when resonances/antiresonances occur in the system. To this end, the structure of the gas flow is summarized in Figures 10-13 where the velocity field v_z is plotted against the distance across the gap of the channel for different periods of oscillation. For a better visualization, the profiles of the stress tensor P_{zz}, the density ρ and the temperature τ are also presented in the same Figures. All the macroscopic fields considered are solutions of the ES kinetic equations. Indeed, when a resonant response of the system occurs, the velocity field of the gas (v_z) takes the form of a standing wave and concomitantly also the P_{zz}-field assumes a characteristic shape, while, for higher values of T, the v_z profile loses its wavy feature and P_{zz} can be considered almost independent of z in each stage during a period of oscillation of the moving wall. Figures 10-13 have been obtained by considering a specific value of the rarefaction parameter ($\delta = 0.1$) but the shape of the macroscopic fields (depicted at different stages during a period of oscillation after the transient behavior has ended) remains qualitatively and quantitatively the same if one changes δ and T in such a way that the ratio δ/T is kept constant.

V. CONCLUDING REMARKS

In the present paper, we have investigated the mechanism responsible for gas damping in Micro-Electro-Mechanical Systems devices vibrating at high frequencies through the kinetic theory of rarefied gases. In particular, a scaling law has been found out, that predicts a resonant response of the system when the ratio between the rarefaction parameter δ and the dimensionless period T of oscillation of the moving wall of the device takes a well-defined fixed value. The theoretical analysis presented in the previous sections can be used for optimizing the working conditions of MEMS devices vibrating at high frequencies. Once the maximum frequency of oscillation of the moving parts of the microdevice has been fixed according to the current capabilities of the RF systems designer, Eq. (50) allows to compute the corresponding δ (that is, the working pressure of the gas) in order to match the antiresonant response of the system and reduce consequently the damping

due to the gas. The feasibility of this approach is pointed out in Fig. 14 which shows the profiles of the normal stress amplitude at the oscillating wall as a function of the rarefaction parameter δ for a given period T (all profiles have been obtained using the ES model). Corresponding to the three values of the period of oscillation T considered, that is $T_a = 31$, $T_a = 62.8$, $T_a = 95$, Eq. (50) predicts an antiresonant response of the system when the rarefaction parameter assumes the following values: $\delta = T_a \cdot L_a \simeq 6.5$, $\delta = T_a \cdot L_a \simeq 13.2$, $\delta = T_a \cdot L_a \simeq 20$, respectively, (where $L_a \simeq 0.21$). On the one hand, Fig. 14 demonstrates once more that the predictions of the scaling law expressed by Eq. (50) agree very well with the numerical results. On the other hand, this picture shows that the gas conditions corresponding to a value of the rarefaction parameter which matches the antiresonant response of the system, at a fixed period T, are the most favourable ones over a wide δ range, since they allow to obtain the lowest value of the damping force exerted by the gas.

Very recently, inertial effects in high-frequency squeezed-film dampers have been modelled by using the linearized Navier-Stokes equations with slip boundary conditions for temperature [11], [12]. The approximate Nth resonant frequency given by T. Veijola and A. Lehtovuori in [11], [12] reads

$$\nu' = \frac{1}{T'} = \frac{N}{4}\,\frac{c}{d} \qquad\qquad N = 1, 2, 3, \ldots \tag{76}$$

where $c = \sqrt{\gamma\, R\, T_0}$ is the adiabatic sound speed with γ being the specific heat ratio, R being the gas constant and T_0 being the equilibrium temperature of the gas. In Eq. (76), odd values of N give antiresonances, while even values of N give resonances. By rewriting Eq. (76) as follows

$$\frac{N}{4} = \frac{d}{c\,T'} \tag{77}$$

and by comparing it with Eq. (50), which in dimensional form reads

$$L = \frac{d}{v_0\,T'} \tag{78}$$

one can conclude that the two formulas (Eqs. (77) and (78)) are closely related since the sound velocity c has the same order as the most probable velocity v_0. Indeed, the values

of the resonant frequencies predicted by the two formulas are not in close quantitative agreement, since the constant fixed values appearing on the left-hand side of Eqs. (77) and (78) are different. This is more clearly seen in the prediction of resonances rather than antiresonances. In fact, for a channel gap d of size equals to $1\,\mu$m in air at atmospheric pressure ($\mathrm{P_a} \simeq 101\,10^3\,\mathrm{N/m^2}$) and ambient temperature ($T_0 \simeq 25^o C$), with a rarefaction parameter δ lying in the near-continuum region ($\delta \simeq 13$), the value predicted by Eq. (77) for the first antiresonance frequency ($\mathrm{N} = 1$)

$$\nu_a \simeq 87.47\,\mathrm{Mhz}$$

shows a good agreement with the value obtained through Eq. (78)

$$\nu_a \simeq 88\,\mathrm{MHz}.$$

Instead, under the same rarefaction conditions ($\delta \simeq 13$) the values given by Eqs. (77) and (78) for the first resonance frequency are not so closely related: By using Eq. (77) with $\mathrm{N} = 2$ one obtains

$$\nu_r \simeq 175\,\mathrm{MHz}$$

while Eq. (78) predicts

$$\nu_r \simeq 185\,\mathrm{MHz}.$$

However, in spite of the good prediction for the exact location of the first antiresonant frequency, the analysis presented by T. Veijola and A. Lehtovuori in [11], [12] fails to give the correct value for the amplitude of the stress tensor at the moving wall (that is the damping force exerted by the gas) even in the near-continuum regime. In fact, it is pointed out in [11] that the damping coefficient estimated by using the Navier-Stokes equations with slip boundary conditions can explain only about a fourth part of the total damping due to air in a RF MEMS disk resonator operating at atmospheric pressure described in [1], [2]. This is likely related to the fact that in [11] the authors do not use the temperature slip coefficient recommended in [26] in order to obtain close results between the kinetic equations and the Navier-Stokes equations in the slip region. But, as

underlined in the previous section, for a rarefaction parameter $\delta > 1$ the thermal effects play an important role in determining the exact location of the resonances as well as the correct amplitude of the normal stress. Of course, to assess more closely the reliability of our theoretical analysis a systematic comparison with experimental results would be highly desirable, but, unfortunately, at the present, a complete experimental data set is still lacking due to technical difficulties in manufacturing microdevices vibrating at high frequencies.

ACKNOWLEDGMENTS

The authors are grateful to GDRE Grefi-Mefi for its financial support. S. Lorenzani also thanks 'Fondazione Cariplo' for the support of her research activity. Moreover, the authors acknowledge Alessandro Caspani for his help in numerical data analysis, Luca Marino for valuable discussions about the experimental observations of sound waves propagation, and both referees for their helpful suggestions to improve the readability of the paper.

APPENDIX: DETAILED FORM OF THE COEFFICIENTS APPEARING IN THE NUMERICAL SCHEME (69)

$$h, k = 0, \dots, n-1$$

$$\alpha_{hk} = \frac{1}{\gamma\sqrt{\pi}}\left[T_0\left(\left(|k-h|\frac{\delta}{n} + \frac{\delta}{2\,n}\right)\gamma\right) - T_0\left(\left(|k-h|\frac{\delta}{n} - \frac{\delta}{2\,n}\right)\gamma\right)\right] + \Gamma_{hk} \qquad (h \neq k)$$

$$\alpha_{kk} = 1 - \frac{1}{\gamma} + \frac{2}{\gamma\sqrt{\pi}}T_0\left(\frac{\delta\,\gamma}{2\,n}\right) + \Gamma_{kk}$$

with

$$\Gamma_{hk} = -\frac{2}{\gamma\sqrt{\pi}}[1-4\,T_1^2(\delta\,\gamma)]^{-1}\left\{\left[T_1\left(\frac{k\,\delta\,\gamma}{n}\right)-T_1\left((k+1)\frac{\delta}{n}\,\gamma\right)\right]\right.$$
$$\times\left[2\,T_1(\delta\,\gamma)\,T_0\left(\left(\delta-(2h+1)\frac{\delta}{2\,n}\right)\gamma\right)+T_0\left((2h+1)\frac{\delta}{2\,n}\gamma\right)\right]$$
$$+\left[T_1\left(\left(\delta-(k+1)\frac{\delta}{n}\right)\gamma\right)-T_1\left(\left(\delta-\frac{k\,\delta}{n}\right)\gamma\right)\right]$$
$$\left.\times\left[T_0\left(\left(\delta-(2h+1)\frac{\delta}{2\,n}\right)\gamma\right)+2\,T_1(\delta\,\gamma)\,T_0\left((2h+1)\frac{\delta}{2\,n}\gamma\right)\right]\right\}$$

$$\alpha_{h,k+n} = -\frac{2}{\gamma\sqrt{\pi}}sgn(k-h)\left[T_1\left(\left(|k-h|\frac{\delta}{n}+\frac{\delta}{2\,n}\right)\gamma\right)-T_1\left(\left(|k-h|\frac{\delta}{n}-\frac{\delta}{2\,n}\right)\gamma\right)\right]$$
$$+\Delta_{hk}\qquad(h\neq k)$$

$$\alpha_{k,k+n} = \Delta_{kk}$$

with

$$\Delta_{hk} = -\frac{4}{\gamma\sqrt{\pi}}[1-4\,T_1^2(\delta\,\gamma)]^{-1}\left\{\left[T_2\left(\left(\delta-(k+1)\frac{\delta}{n}\right)\gamma\right)-T_2\left(\left(\delta-\frac{k\,\delta}{n}\right)\gamma\right)\right]\right.$$
$$\times\left[T_0\left(\left(\delta-(2h+1)\frac{\delta}{2\,n}\right)\gamma\right)+2\,T_1(\delta\,\gamma)\,T_0\left((2h+1)\frac{\delta}{2\,n}\,\gamma\right)\right]$$
$$-\left[T_2\left(\frac{k\,\delta}{n}\,\gamma\right)-T_2\left((k+1)\frac{\delta}{n}\,\gamma\right)\right]\times\left[2\,T_1(\delta\,\gamma)\,T_0\left(\left(\delta-(2h+1)\frac{\delta}{2\,n}\right)\gamma\right)\right.$$
$$\left.\left.+T_0\left((2h+1)\frac{\delta}{2\,n}\,\gamma\right)\right]\right\}$$

$$\alpha_{h+n,k} = -\frac{1}{\gamma\sqrt{\pi}}sgn(k-h)\left[T_1\left(\left(|k-h|\frac{\delta}{n}+\frac{\delta}{2\,n}\right)\gamma\right)-T_1\left(\left(|k-h|\frac{\delta}{n}-\frac{\delta}{2\,n}\right)\gamma\right)\right]$$
$$+\Lambda_{hk}\qquad(h\neq k)$$

$$\alpha_{k+n,k} = \Lambda_{kk}$$

with

$$\Lambda_{hk} = \frac{2}{\gamma\sqrt{\pi}}[1 - 4\,T_1^2(\delta\,\gamma)]^{-1}\left\{\left[T_1\left(\frac{k\,\delta}{n}\,\gamma\right) - T_1\left((k+1)\frac{\delta}{n}\,\gamma\right)\right]\right.$$
$$\times\left[2\,T_1(\delta\,\gamma)\,T_1\left(\left(\delta - (2h+1)\frac{\delta}{2\,n}\right)\gamma\right) - T_1\left((2h+1)\frac{\delta}{2\,n}\,\gamma\right)\right]$$
$$+\left[T_1\left(\left(\delta - (k+1)\frac{\delta}{n}\right)\gamma\right) - T_1\left(\left(\delta - \frac{k\,\delta}{n}\right)\gamma\right)\right]$$
$$\left.\times\left[T_1\left(\left(\delta - (2h+1)\frac{\delta}{2\,n}\right)\gamma\right) - 2\,T_1(\delta\,\gamma)\,T_1\left((2h+1)\frac{\delta}{2\,n}\,\gamma\right)\right]\right\}$$

$$\alpha_{h+n,k+n} = \frac{2}{\gamma\sqrt{\pi}}\left[T_2\left(\left(|k-h|\frac{\delta}{n} + \frac{\delta}{2\,n}\right)\gamma\right) - T_2\left(\left(|k-h|\frac{\delta}{n} - \frac{\delta}{2\,n}\right)\gamma\right)\right]$$
$$+\,\Pi_{hk} \qquad (h \neq k)$$

$$\alpha_{k+n,k+n} = 1 - \frac{1}{\gamma} + \frac{4}{\gamma\sqrt{\pi}}T_2\left(\frac{\delta\,\gamma}{2\,n}\right) + \Pi_{kk}$$

with

$$\Pi_{hk} = \frac{4}{\gamma\sqrt{\pi}}[1 - 4\,T_1^2(\delta\,\gamma)]^{-1}\left\{\left[T_2\left(\left(\delta - (k+1)\frac{\delta}{n}\right)\gamma\right) - T_2\left(\left(\delta - \frac{k\,\delta}{n}\right)\gamma\right)\right]\right.$$
$$\times\left[T_1\left(\left(\delta - (2h+1)\frac{\delta}{2\,n}\right)\gamma\right) - 2\,T_1(\delta\,\gamma)\,T_1\left((2h+1)\frac{\delta}{2\,n}\,\gamma\right)\right]$$
$$+\left[T_2\left(\frac{k\,\delta}{n}\,\gamma\right) - T_2\left((k+1)\frac{\delta}{n}\,\gamma\right)\right]\times\left[T_1\left((2h+1)\frac{\delta}{2\,n}\,\gamma\right)\right.$$
$$\left.\left.- 2\,T_1(\delta\,\gamma)\,T_1\left(\left(\delta - (2h+1)\frac{\delta}{2\,n}\right)\gamma\right)\right]\right\}$$

$$\beta_h = \frac{2}{\sqrt{\pi}}\,T_1\left((2h+1)\frac{\delta}{2\,n}\,\gamma\right) + \frac{1}{\sqrt{\pi}}[1 - 4\,T_1^2(\delta\,\gamma)]^{-1}\times\left\{T_0\left(\left(\delta - (2h+1)\frac{\delta}{2\,n}\right)\gamma\right)\right.$$
$$\left.\times\left[2\sqrt{\pi}\,T_1(\delta\,\gamma) + 4\,T_2(\delta\,\gamma)\right] + T_0\left((2h+1)\frac{\delta}{2\,n}\,\gamma\right)\times\left[\sqrt{\pi} + 8\,T_1(\delta\,\gamma)\,T_2(\delta\,\gamma)\right]\right\}$$

$$\beta_{h+n} = \frac{2}{\sqrt{\pi}}\,T_2\left((2h+1)\frac{\delta}{2\,n}\,\gamma\right) - \frac{1}{\sqrt{\pi}}[1 - 4\,T_1^2(\delta\,\gamma)]^{-1}\times\left\{T_1\left(\left(\delta - (2h+1)\frac{\delta}{2\,n}\right)\gamma\right)\right.$$
$$\left.\times\left[2\sqrt{\pi}\,T_1(\delta\,\gamma) + 4\,T_2(\delta\,\gamma)\right] - T_1\left((2h+1)\frac{\delta}{2\,n}\,\gamma\right)\times\left[\sqrt{\pi} + 8\,T_1(\delta\,\gamma)\,T_2(\delta\,\gamma)\right]\right\}$$

[1] J. R. Clark, W.-T. Hsu, and C. T.-C. Nguyen, "High-Q VHF Micromechanical Contour-Mode Disk Resonators," Technical Digest, IEEE Int. Electron Devices Meeting, San Francisco, California, Dec. 10-13, pp. 493-496 (2000). DOI: 10.1109/IEDM.2000.904363.

[2] B. Bircumshaw, G. Liu, H. Takeuchi, T.-J. King, R. Howe, O. O'Reilly, and A. Pisano, "The radial bulk annular resonator: Towards a 50Ω RF MEMS filter," Proceedings of the 12th International conference on Transducers, Solid-State Sensors, Actuators and Microsystems, Boston, June 9-12, Vol. 1, pp. 875-878 (2003). DOI: 10.1109/SENSOR.2003.1215614.

[3] Z. Hao, S. Pourkamali, and F. Ayazi, "VHF Single-Crystal Silicon Elliptic Bulk-Mode Capacitive Disk Resonators-Part I: Design and Modeling," Journal of Microelectromechanical Systems **13**, 1043 (2004).

[4] S. Pourkamali, Z. Hao, and F. Ayazi, "VHF Single-Crystal Silicon Capacitive Elliptic Bulk-Mode Disk Resonators-Part II: Implementation and Characterization," Journal of Microelectromechanical Systems **13**, 1054 (2004).

[5] J. R. Clark, W.-T. Hsu, M. A. Abdelmoneum, and C. T.-C. Nguyen, "High-Q UHF Micromechanical Radial-Contour Mode Disk Resonators," Journal of Microelectromechanical Systems **14**, 1298 (2005).

[6] Y. Cho, A. P. Pisano, and R. T. Howe, "Viscous damping model for laterally oscillating microstructures," Journal of Microelectromechanical Systems **3**, 81 (1994).

[7] T. Veijola, H. Kuisma, J. Lahdenperä, and T. Ryhänen, "Equivalent-circuit model of the squeezed gas film in a silicon accelerometer," Sens. Actuators A **48**, 239 (1995).

[8] T. Veijola, H. Kuisma, and J. Lahdenperä, "The influence of gas-surface interaction on gas-film damping in a silicon accelerometer," Sens. Actuators A **66**, 83 (1998).

[9] A. Frangi, A. Frezzotti, and S. Lorenzani, "On the application of the BGK kinetic model to the analysis of gas-structure interactions in MEMS," Computers and Structures **85**, 810 (2007).

[10] C. Cercignani, A. Frangi, S. Lorenzani, and B. Vigna, "BEM approaches and simplified kinetic models for the analysis of damping in deformable MEMS," Eng. Anal. Boundary Elem. **31**, 451 (2007).

[11] T. Veijola and A. Lehtovuori, "Model for gas damping in air gaps of RF MEMS resonators," in *Symposium on Design, Test, Integration and Packaging of MEMS/MOEMS*. EDA publishing/DTIP 2007, Stresa, Italy, April 25-27, pp. 156-161 (2007). ISBN: 978-2-35500-000-3.

[12] T. Veijola and A. Lehtovuori, "Numerical and analytical modelling of trapped gas in micromechanical squeeze-film dampers," Journal of Sound and Vibration **319**, 606 (2009).

[13] C. Cercignani, *The Boltzmann Equation and Its Applications* (Springer, New York, 1988).

[14] Y. Sone, *Molecular Gas Dynamics: Theory, Techniques, and Applications* (Birkhäuser, Boston, 2007).

[15] P. L. Bhatnagar, E. P. Gross, and M. Krook, "A model for collision processes in gases. I. Small amplitude processes in charged and neutral one-component systems," Phys. Rev. **94**, 511 (1954).

[16] F. Sharipov and V. Seleznev, "Data on internal rarefied gas flows," J. Phys. Chem. Ref. Data **27**, 657 (1999).

[17] L. B. Barichello, M. Camargo, P. Rodrigues, and C. E. Siewert, "Unified solutions to classical flow problems based on the BGK model," Z. Angew. Math. Phys. **52**, 517 (2001).

[18] L. H. Holway, "New statistical models for kinetic theory: methods of construction," Phys. Fluids **9**, 1658 (1966).

[19] C. Cercignani and G. Tironi, "Some applications of a linearized kinetic model with correct Prandtl number," Il Nuovo Cimento **43**, 64 (1966).

[20] C. Cercignani, M. Lampis, and S. Lorenzani, "On the Reynolds equation for linearized models of the Boltzmann operator," Transp. Theory Stat. Phys. **36**, 257 (2007).

[21] S. K. Loyalka and T. C. Cheng, "Sound-wave propagation in a rarefied gas," Phys. Fluids **22**, 830 (1979).

[22] M. M. R. Williams, "A review of the rarefied gas dynamics theory associated with some classical problems in flow and heat transfer," Z. Angew. Math. Phys. **52**, 500 (2001).

[23] R. D. M. Garcia and C. E. Siewert, "The linearized Boltzmann equation: Sound-wave propagation in a rarefied gas," Z. Angew. Math. Phys. **57**, 94 (2006).

[24] A. B. Huang and D. L. Hartley, "Nonlinear rarefied Couette flow with heat transfer," Phys. Fluids **11**, 1321 (1968).

[25] S. Naris and D. Valougeorgis, "The driven cavity flow over the whole range of the Knudsen

number," Physics of Fluids **17**, 097106 (2005).

[26] D. Kalempa and F. Sharipov, "Sound propagation through a rarefied gas confined between source and receptor at arbitrary Knudsen number and sound frequency," Physics of Fluids **21**, 103601 (2009).

[27] S. Lorenzani, L. Gibelli, A. Frezzotti, A. Frangi, and C. Cercignani, "Kinetic approach to gas flows in microchannels," Nanoscale Microscale Thermophys. Eng. **11**, 211 (2007).

[28] N. G. Hadjiconstantinou and A. L. Garcia, "Molecular simulations of sound wave propagation in simple gases," Physics of Fluids **13**, 1040 (2001).

[29] N. G. Hadjiconstantinou, "Sound wave propagation in transition-regime micro- and nanochannels," Physics of Fluids **14**, 802 (2002).

[30] C. Cercignani and A. Daneri, "Flow of a rarefied gas between two parallel plates," J. Appl. Phys. **34**, 3509 (1963).

[31] C. Cercignani, M. Lampis, and S. Lorenzani, "Plane Poiseuille-Couette problem in micro-electro-mechanical systems applications with gas-rarefaction effects," Physics of Fluids **18**, 087102 (2006).

TABLE I. Amplitude of P_{zz} at $z = -\delta/2$. Comparison between our results, obtained through a numerical integration of the BGK and ES model equations, and those presented in [26].

	$T = 0.6283$			$T = 6.283$			$T = 62.83$		
δ	([26])	BGK	ES	([26])	BGK	ES	([26])	BGK	ES
0.1	0.6255	0.6226	0.6206	5.234	4.909	4.957	47.59	46.93	47.09
0.5	0.9709	0.9682	0.9703	1.176	1.158	1.168	10.04	9.83	9.87
1.0	1.008	1.007	1.007	0.5337	0.5303	0.5267	5.039	4.966	4.990
2.0	1.006	1.007	1.007	0.7686	0.7773	0.7830	2.456	2.528	2.534
4.0	1.007	1.007	1.007	0.9645	0.9513	0.9498	1.313	1.333	1.313
6.0	1.007	1.007	1.007	0.9695	0.9869	0.9808	0.8822	0.9070	0.8812
8.0	1.007	1.007	1.007	0.9553	0.9507	0.9546	0.6156	0.6275	0.6117
10.0	1.007	1.007	1.007	0.9617	0.9668	0.9646	0.4045	0.4034	0.3990

TABLE II. Absolute value of the phase of P_{zz} at $z = -\delta/2$. Comparison between our results, obtained through a numerical integration of the BGK and ES model equations, and those presented in [26].

	$T = 0.6283$			$T = 6.283$			$T = 62.83$		
δ	([26])	BGK	ES	([26])	BGK	ES	([26])	BGK	ES
0.1	0.8106	0.8091	0.8108	1.402	1.404	1.404	1.548	1.552	1.551
0.5	0.07301	0.07694	0.07466	1.092	1.090	1.102	1.505	1.504	1.501
1.0	0.005634	0.004545	0.005102	0.7191	0.7135	0.7240	1.460	1.457	1.455
2.0	0.01087	0.00950	0.00959	0.6391	0.6370	0.6372	1.383	1.375	1.377
4.0	0.01085	0.00950	0.00959	0.07664	0.10217	0.08229	1.259	1.250	1.255
6.0	0.01085	0.00950	0.00959	0.1187	0.1178	0.1089	1.183	1.194	1.183
8.0	0.01085	0.00950	0.00959	0.06595	0.06962	0.06754	1.126	1.159	1.126
10.0	0.01085	0.00950	0.00959	0.07916	0.08155	0.08255	1.020	1.069	1.018

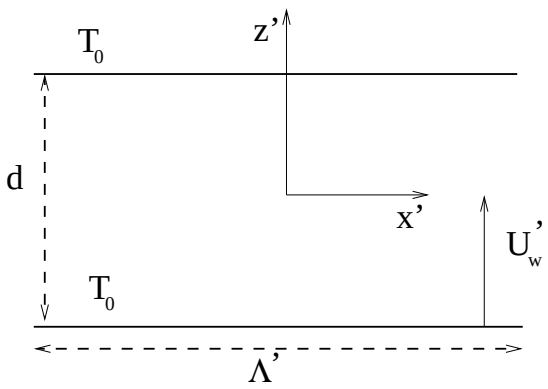

FIG. 1. Channel geometry.

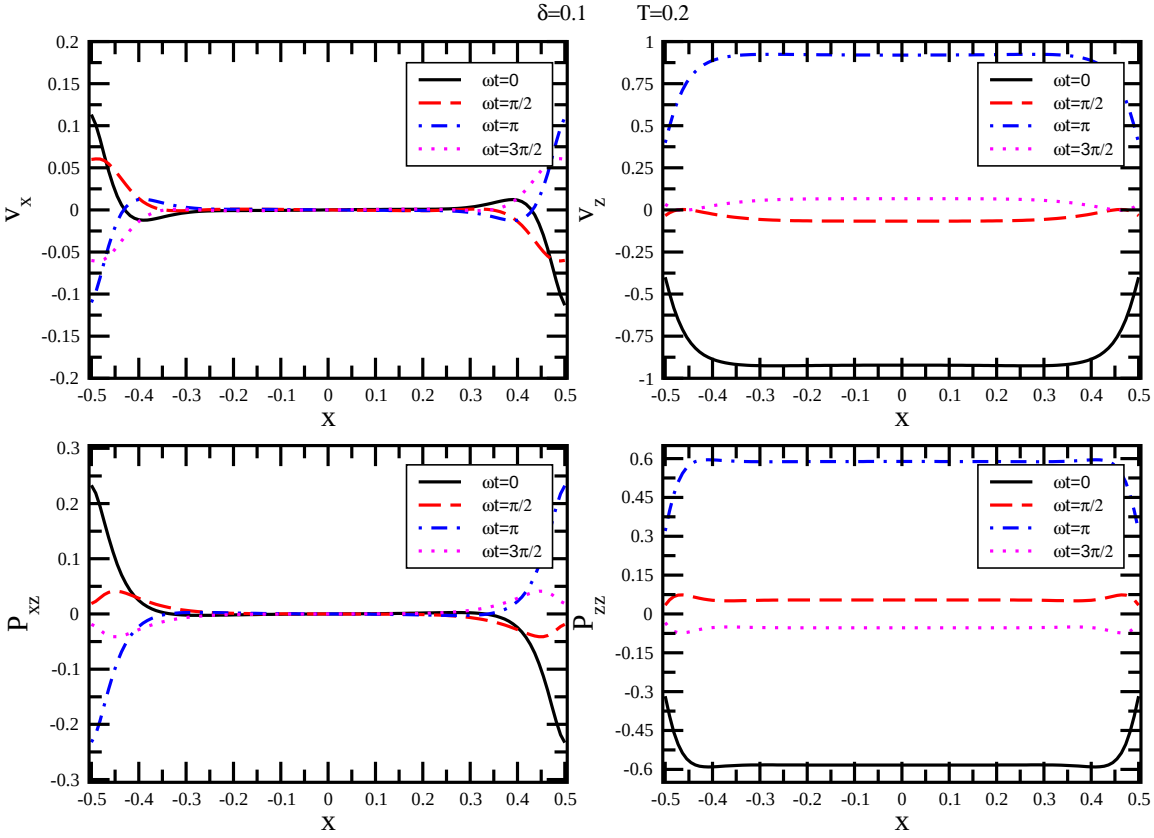

FIG. 2. Variation of the perturbed velocity (v_x, v_z) and stress tensor (P_{xz}, P_{zz}) fields (obtained using the ES model) along the channel for $\delta = 0.1$ and $T = 0.2$. In each panel, the profiles of the macroscopic quantities are shown at different stages during a period of oscillation of the moving wall.

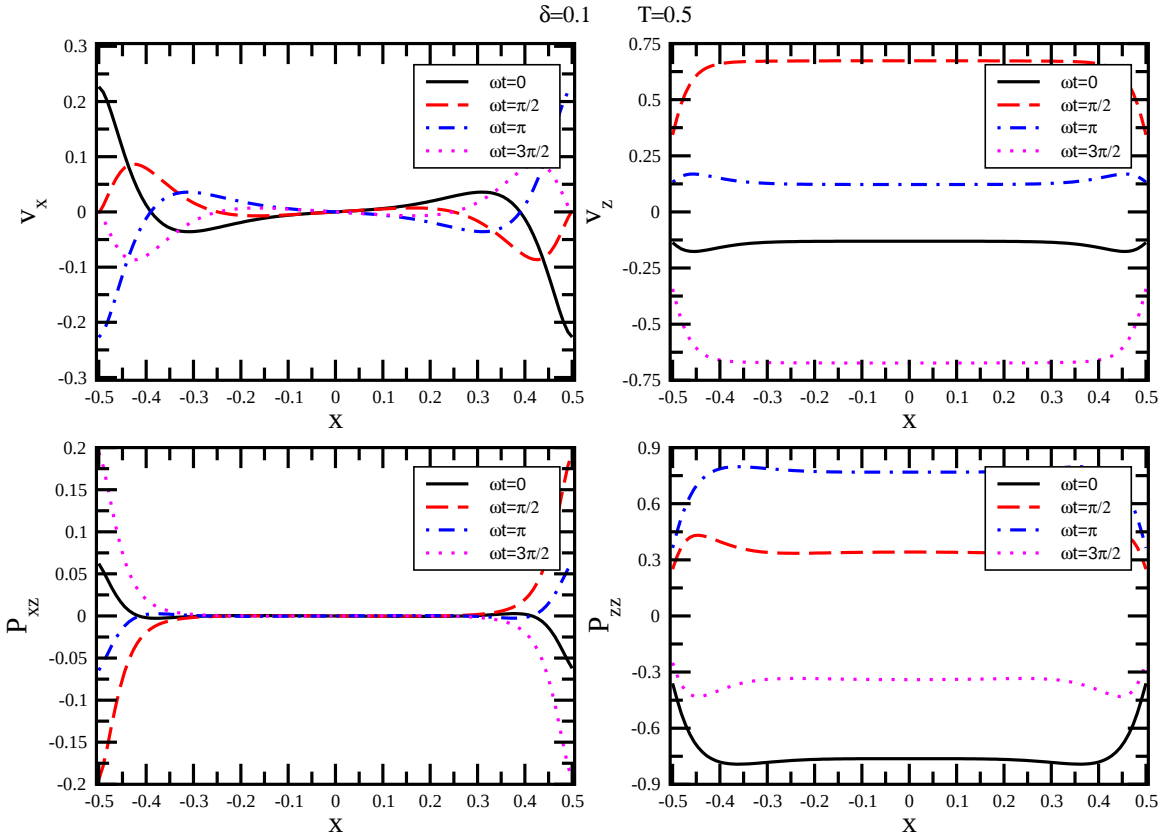

FIG. 3. Variation of the perturbed velocity (v_x, v_z) and stress tensor (P_{xz}, P_{zz}) fields (obtained using the ES model) along the channel for $\delta = 0.1$ and $T = 0.5$. In each panel, the profiles of the macroscopic quantities are shown at different stages during a period of oscillation of the moving wall.

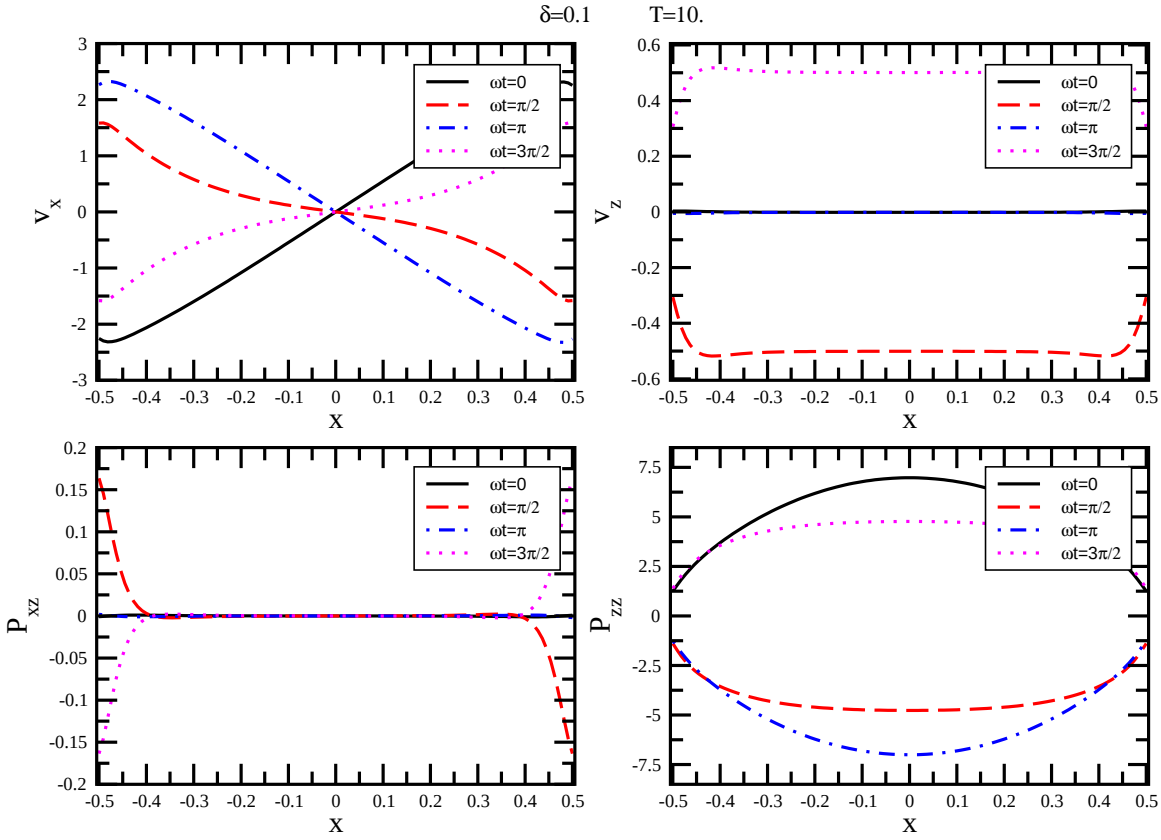

FIG. 4. Variation of the perturbed velocity (v_x, v_z) and stress tensor (P_{xz}, P_{zz}) fields (obtained using the ES model) along the channel for $\delta = 0.1$ and $T = 10$. In each panel, the profiles of the macroscopic quantities are shown at different stages during a period of oscillation of the moving wall.

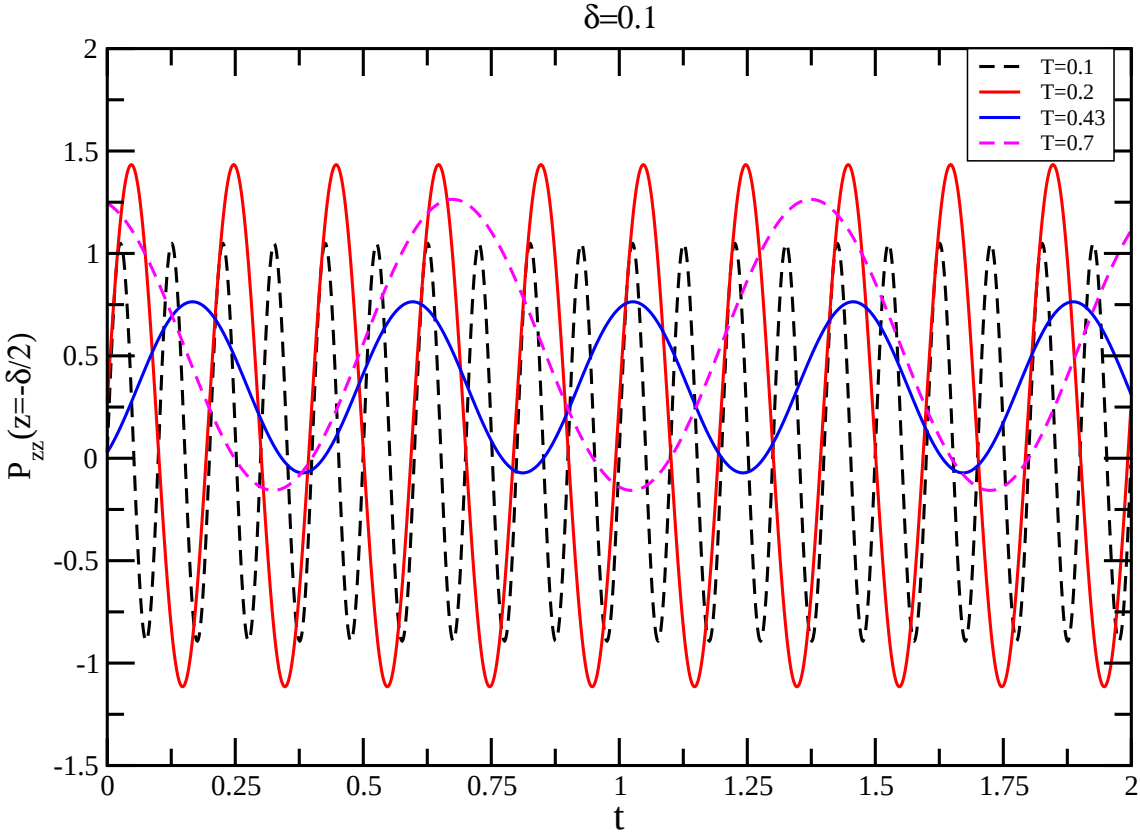

FIG. 5. Temporal evolution of the normal stress P_{zz} at $z = -\delta/2$ (obtained using the ES model) for different periods T of oscillation of the moving wall and a fixed value of the rarefaction parameter $\delta = 0.1$.

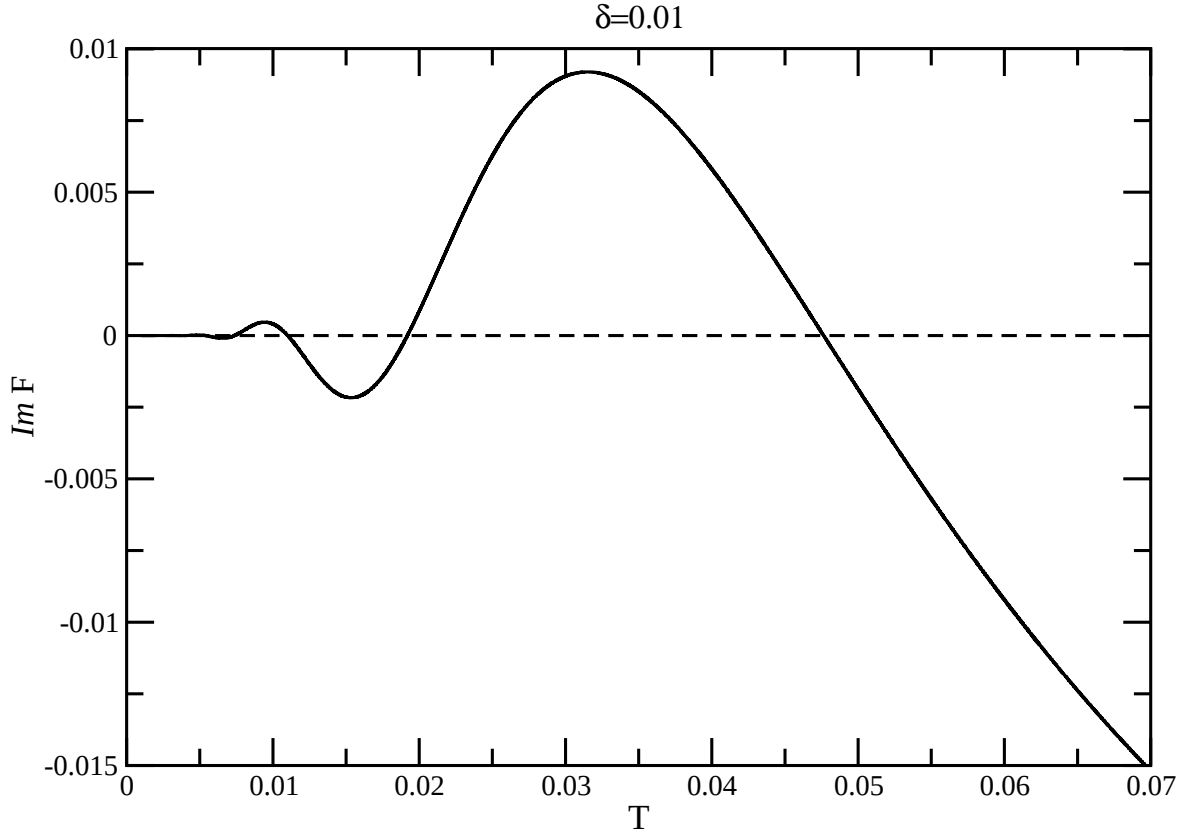

FIG. 6. Imaginary part of the function F, given by Eq. (73), versus the period T of oscillation of the moving wall, for a fixed value of the rarefaction parameter $\delta = 0.01$.

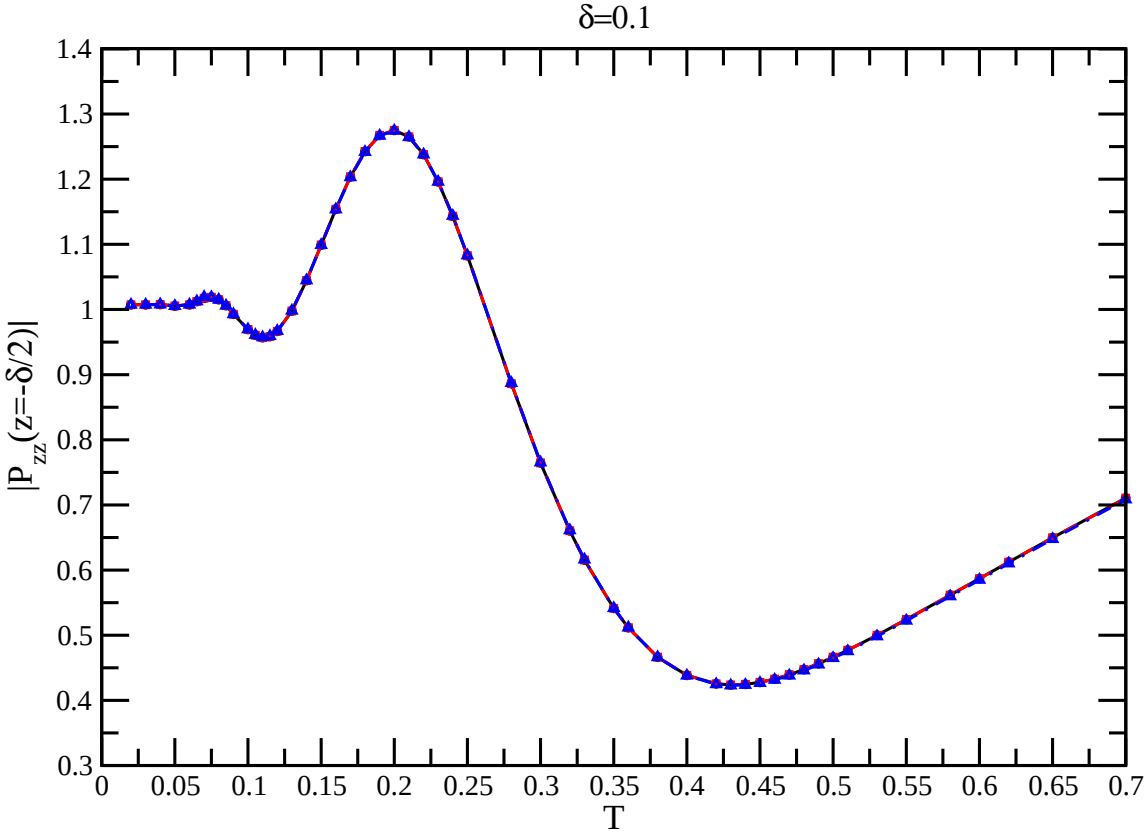

FIG. 7. Amplitude of the normal stress tensor P_{zz} at the oscillating wall versus T for $\delta = 0.1$. Comparison between the results obtained through the ES model (triangles), the BGK model (circles) and the numerical solution of Eq. (51) (squares).

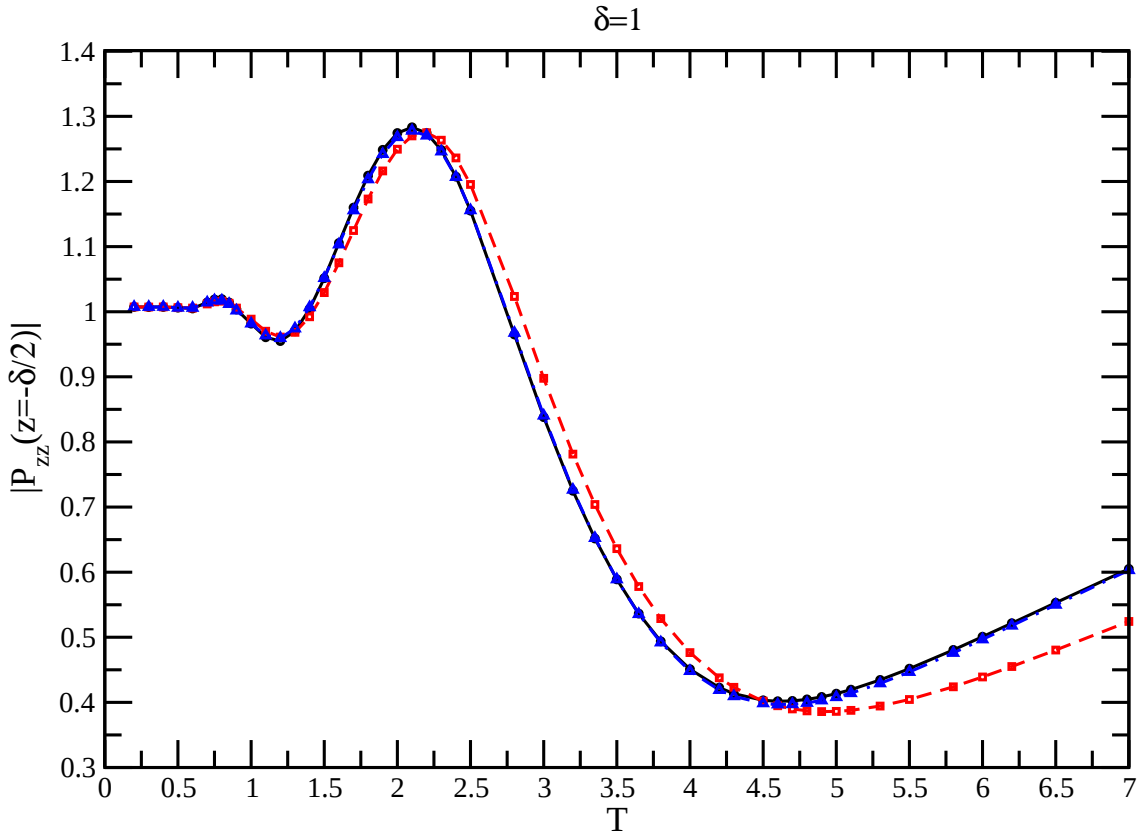

FIG. 8. Amplitude of the normal stress tensor P_{zz} at the oscillating wall versus T for $\delta = 1$. Comparison between the results obtained through the ES model (triangles), the BGK model (circles) and the numerical solution of Eq. (51) (squares).

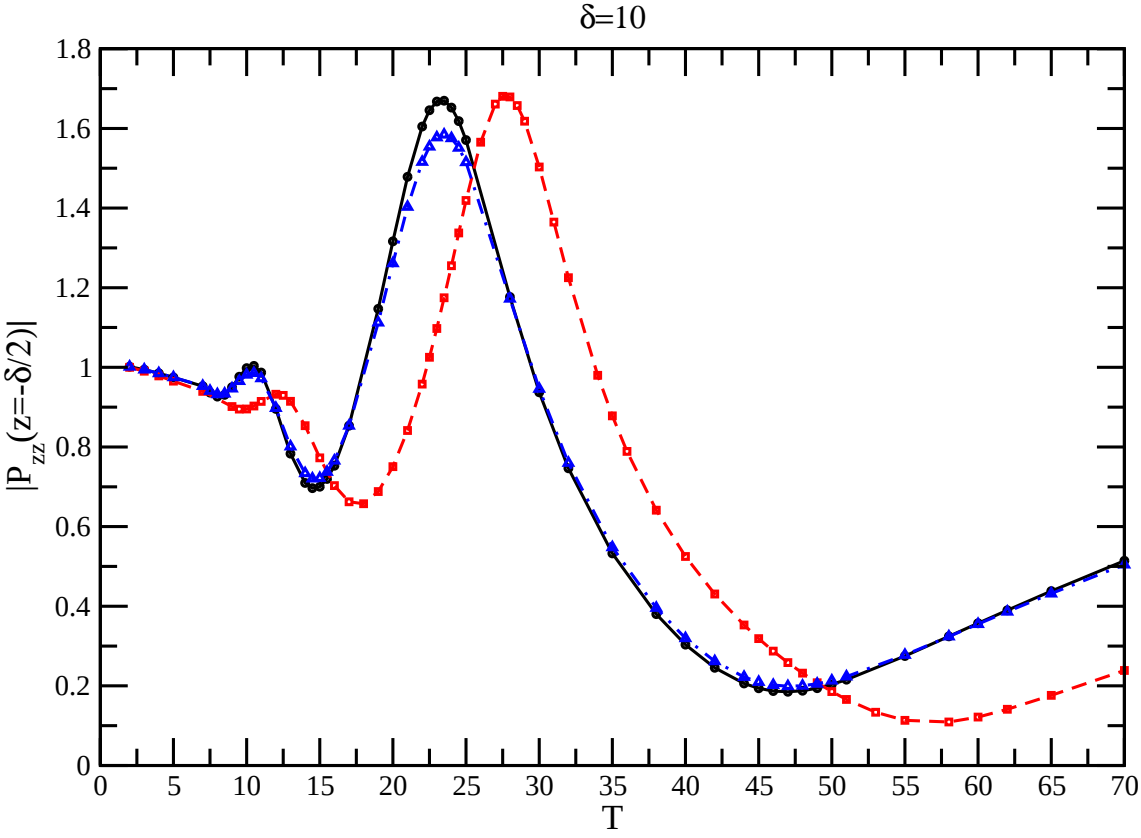

FIG. 9. Amplitude of the normal stress tensor P_{zz} at the oscillating wall versus T for $\delta = 10$. Comparison between the results obtained through the ES model (triangles), the BGK model (circles) and the numerical solution of Eq. (51) (squares).

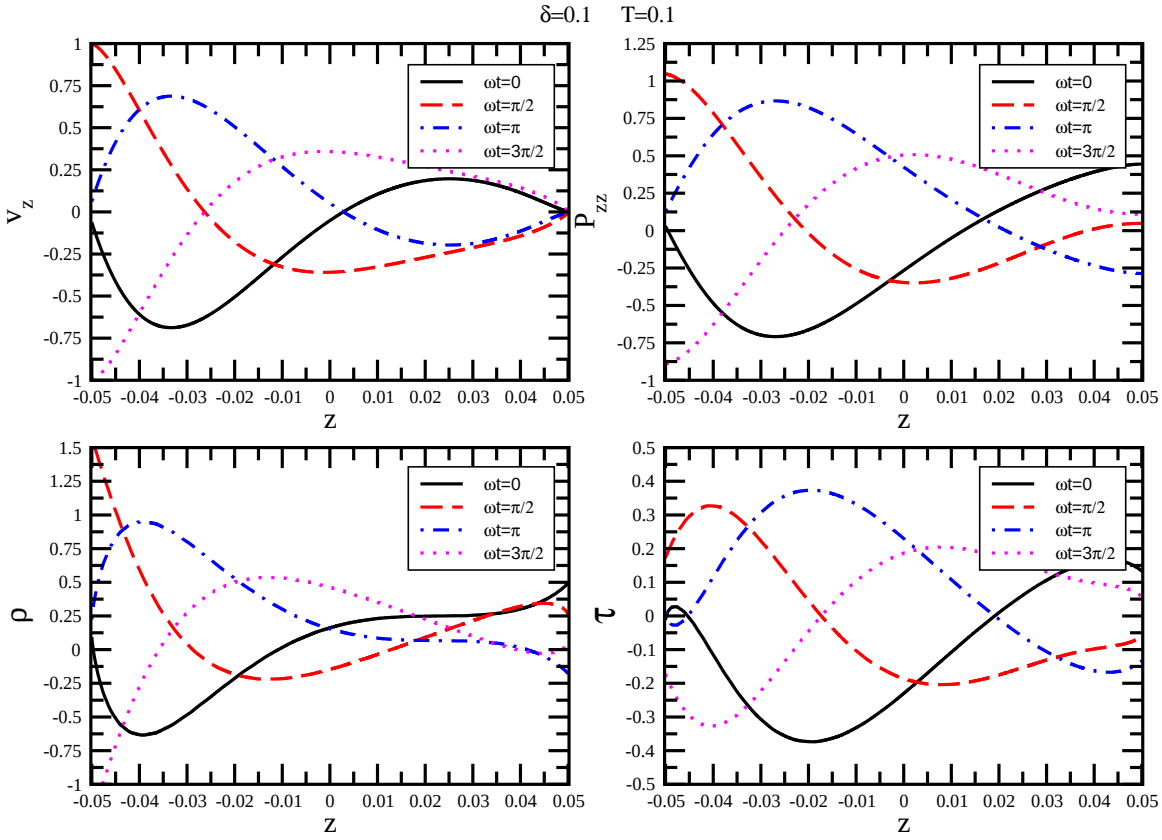

FIG. 10. Variation of the macroscopic perturbed velocity v_z, stress tensor P_{zz}, density ρ, temperature τ (obtained using the ES model) in the z-direction across the gap of the channel for $\delta = 0.1$ and $T = 0.1$. In each panel, the profiles of the macroscopic quantities are shown at different stages during a period of oscillation of the moving wall.

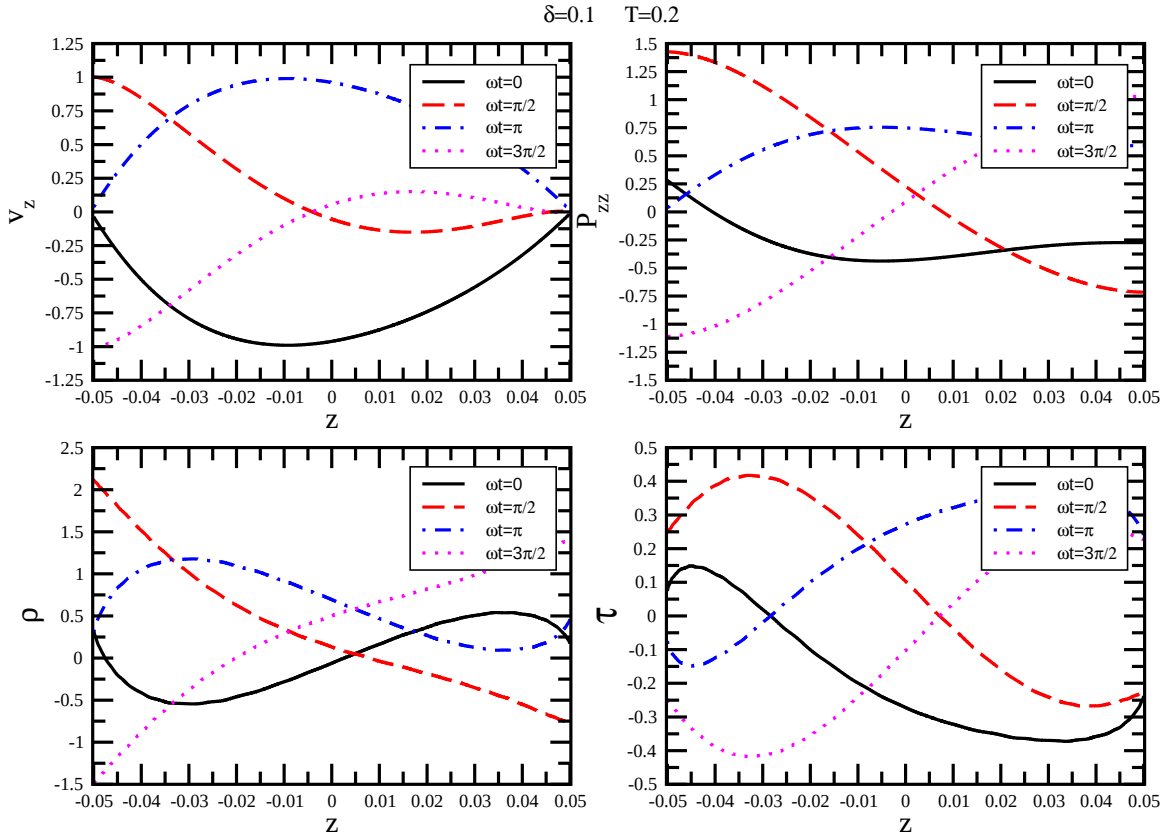

FIG. 11. Variation of the macroscopic perturbed velocity v_z, stress tensor P_{zz}, density ρ, temperature τ (obtained using the ES model) in the z-direction across the gap of the channel for $\delta = 0.1$ and $T = 0.2$. In each panel, the profiles of the macroscopic quantities are shown at different stages during a period of oscillation of the moving wall.

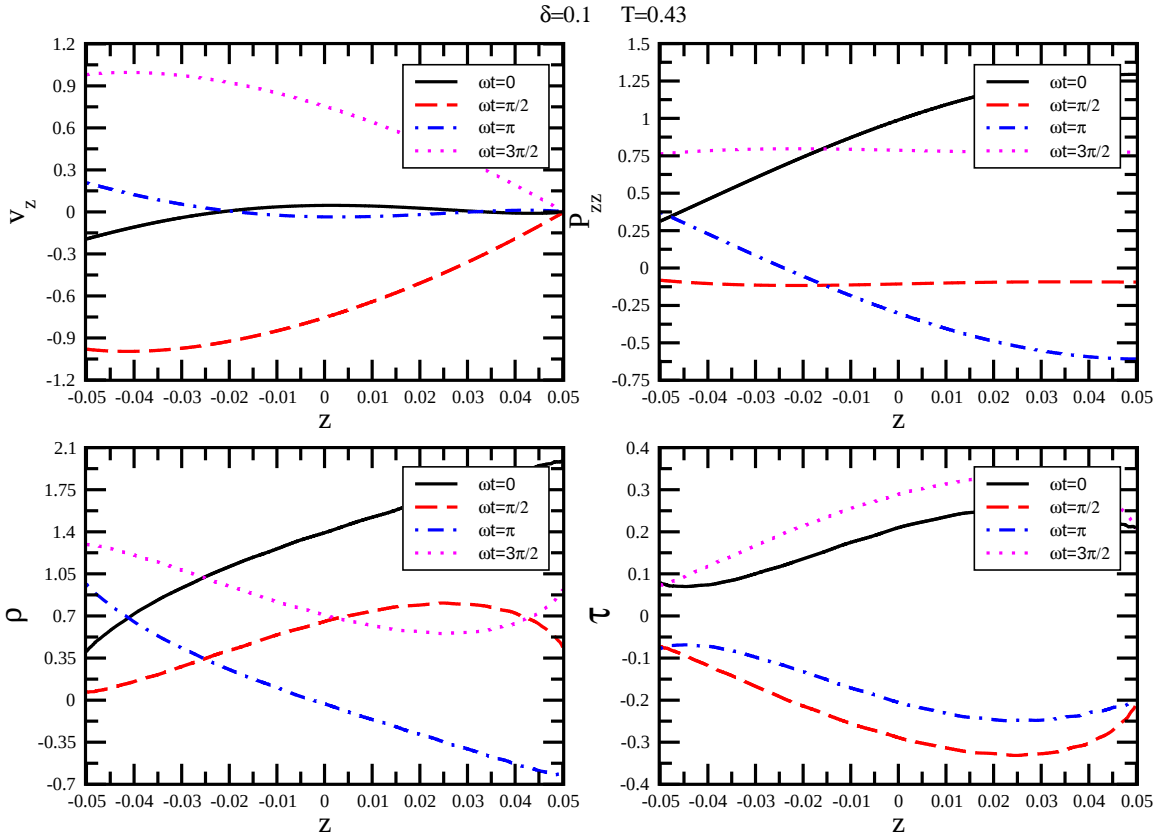

FIG. 12. Variation of the macroscopic perturbed velocity v_z, stress tensor P_{zz}, density ρ, temperature τ (obtained using the ES model) in the z-direction across the gap of the channel for $\delta = 0.1$ and $T = 0.43$. In each panel, the profiles of the macroscopic quantities are shown at different stages during a period of oscillation of the moving wall.

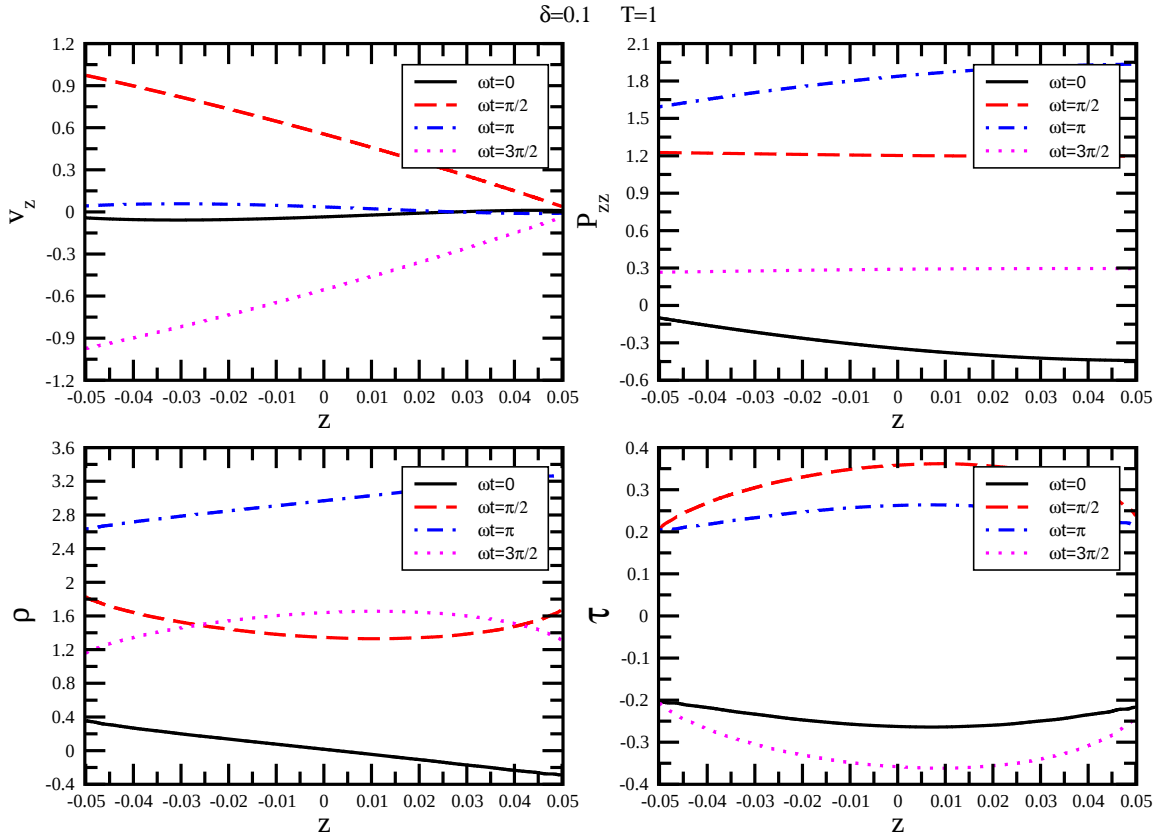

FIG. 13. Variation of the macroscopic perturbed velocity v_z, stress tensor P_{zz}, density ρ, temperature τ (obtained using the ES model) in the z-direction across the gap of the channel for $\delta = 0.1$ and $T = 1$. In each panel, the profiles of the macroscopic quantities are shown at different stages during a period of oscillation of the moving wall.

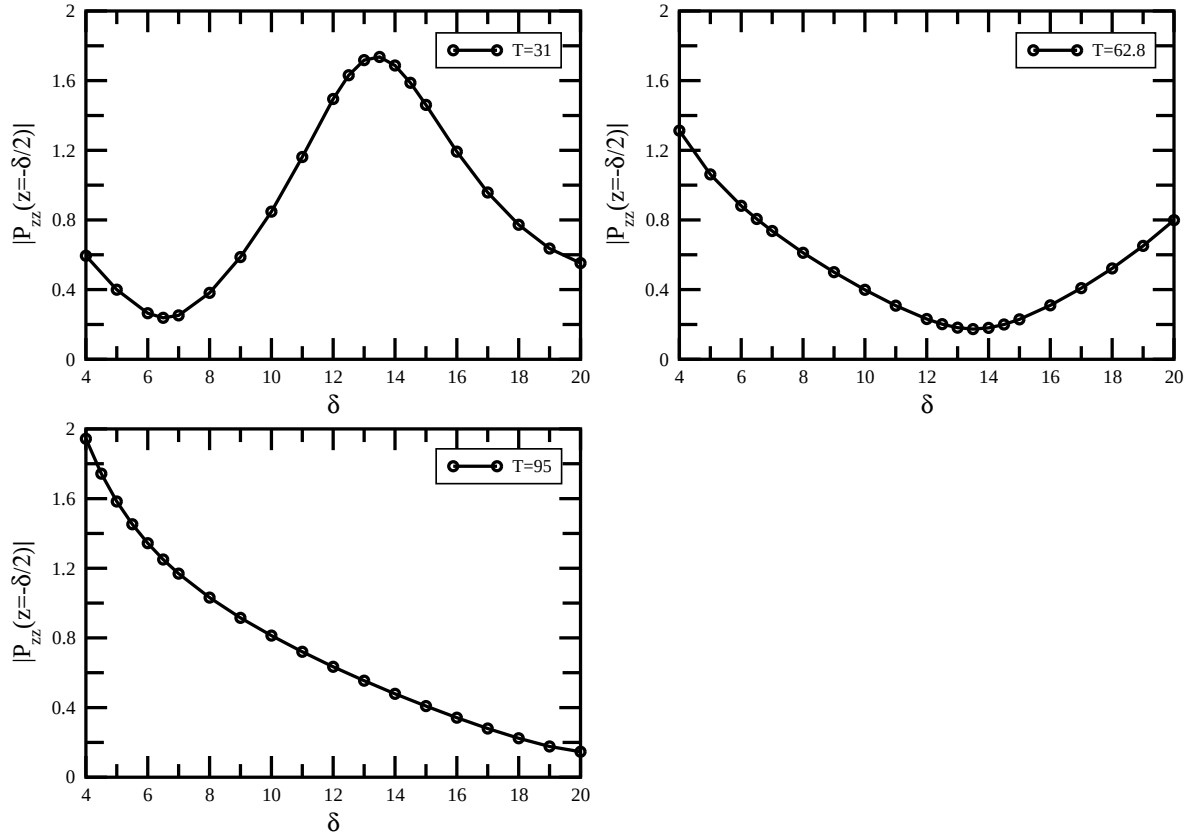

FIG. 14. Amplitude of the normal stress tensor P_{zz} at the oscillating wall versus δ for three different values of T. All profiles have been obtained using the ES model.